IOPscience iopscience.iop.org

This content has been downloaded from IOPscience. Please scroll down to see the full text.

Download details:

IP Address: 18.117.73.223
This content was downloaded on 26/04/2024 at 04:30

Please note that terms and conditions apply.

You may also like:

Gas-Phase Chemistry in Space

Advances in Modern Sensors

The Accretion History of AGN: A Newly Defined Population of Cold Quasars
Allison Kirkpatrick, C. Megan Urry, Jason Brewster et al.

JWST Mid-infrared Spectroscopy Resolves Gas, Dust, and Ice in Young Stellar Objects in the Large Magellanic Cloud
Omnarayani Nayak, Alec S. Hirschauer, Patrick J. Kavanagh et al.

Extension of HOPS out to 500 pc (eHOPS). I. Identification and Modeling of Protostars in the Aquila Molecular Clouds
Riwaj Pokhrel, S. Thomas Megeath, Robert A. Gutermuth et al.

AAS | IOP Astronomy

Dust in the Galactic Environment (Third Edition)

D C B Whittet

Chapter 8

The Life Cycle of Dust—I. Circumstellar Origins

The life cycles of stars and dust are closely linked (see Section 1.4.5 for an overview). In this chapter, we focus on old stars as sources of new grain material. The atmospheres and winds of luminous stars such as red giants and supergiants contain environments conducive to the nucleation and growth of refractory dust grains ("stardust"). Depending on the mass and evolutionary status of the star, the condensates may be carbon-rich or oxygen-rich, and grain formation may occur over extended periods lasting a million years or very rapidly in a cataclysmic event such as a nova or supernova outburst. Periods of grain formation are typically accompanied by episodes of copious mass-loss, generating dusty outflows that merge into the surrounding interstellar medium. A striking example is illustrated in Figure 8.1.

This chapter begins with a review of the physical conditions and chemical processes that control the formation of dust in circumstellar environments (Section 8.1). Stardust research is a domain in which astronomical observations and laboratory studies of extraterrestrial materials are complementary and highly synergistic: results from these areas of investigation are reviewed in Sections 8.2 and 8.3, respectively. A vital and persistent question concerns whether stellar outflows represent a dominant or relatively modest contribution to the total inventory of interstellar dust. The available evidence is reviewed in the final section.

8.1 Dust Formation in Stellar Outflows

8.1.1 Theoretical Basis

Dust formation in stellar atmospheres was first discussed in response to emerging evidence for its presence in the circumstellar environments of stars with low surface temperatures (see Bode 1988 for a review of early work). Luminous stars located in the upper right-hand region of the Hertzsprung–Russell diagram (Figure 8.2) were implicated. Subsequent research has identified asymptotic giant branch (AGB) stars and core-collapse supernovae as major sources, corresponding to the most prolific

doi:10.1088/2514-3433/ac7204ch8 © IOP Publishing Ltd 2022

Figure 8.1. Composite portrait of the planetary nebula NGC 6302 (the Butterfly Nebula), combining UV and visible-light images obtained by the Wide Field Camera 3 of the Hubble Space Telescope. Filters are used to isolate individual spectral lines diagnostic of physical conditions in the gas (Kastner et al. 2022). The nebula contains matter ejected from a central star at speeds of up to ~ 600 km s^{-1} over a period of at least 2000 years, as the star evolved from the asymptotic giant branch to become a hot white dwarf. The star is hidden from view behind a dusty equatorial disk that constricts the outflow, resulting in the nebula's bipolar structure. White areas in the image trace gas energized by shocks, attributed to recent, fast-moving ejecta that overtakes and collides with slower-moving matter ejected during an earlier phase of the star's evolution. Image credit: NASA/ESA/Hubble Space Telescope.

phases of dust production for stars of intermediate (1–8 $M_\odot$) and high (>8 $M_\odot$) initial mass, respectively (Höfner & Olofsson 2018; Sarangi et al. 2018).

We begin by considering the nature of circumstellar matter around a dust-forming red giant (discussion specific to supernovae is differed to Section 8.1.6). A schematic illustration of an AGB star and its environment is shown in Figure 8.3. Elemental C and O are produced by internal nucleosynthesis and mixed into the convective envelope. Taking the center of the star as the origin, the stellar surface (photosphere) is located at radial distance $r = R_*$, and the surrounding atmosphere is subject to dynamical disturbances caused by stellar pulsations and shocks. The atmospheric layer immediately above the photosphere may contain a chromosphere, in which the gas is substantially hotter than in the photosphere (e.g., Gail & Sedlmayr 1987; Guerrero & Ortiz 2020), but at greater distances the temperature is

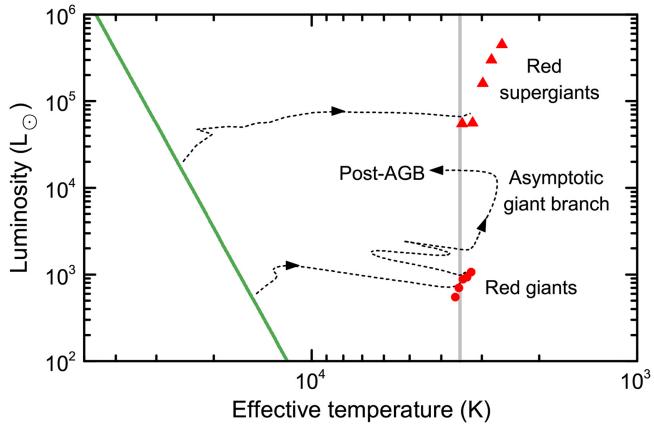

Figure 8.2. Hertzsprung–Russell diagram (effective temperature versus luminosity) showing the post-main-sequence evolution of typical stars that may form dust in their outflows. The main sequence is shown in green, and the dashed curves are evolutionary tracks for single stars of masses 5 $M_\odot$ (below) and 15 $M_\odot$ (above). Red symbols are mean loci for stars in the standard spectral-type sequence from M2 to M6 for giants (luminosity class III, circles) and supergiants (luminosity class I, triangles). The vertical gray line indicates an effective temperature of 3500 K, below which stars typically begin to make dust. A 5 $M_\odot$ star may cross this threshold briefly during its initial (first ascent) red giant phase, but the principal episode of dust production occurs later when it reaches the asymptotic giant branch.

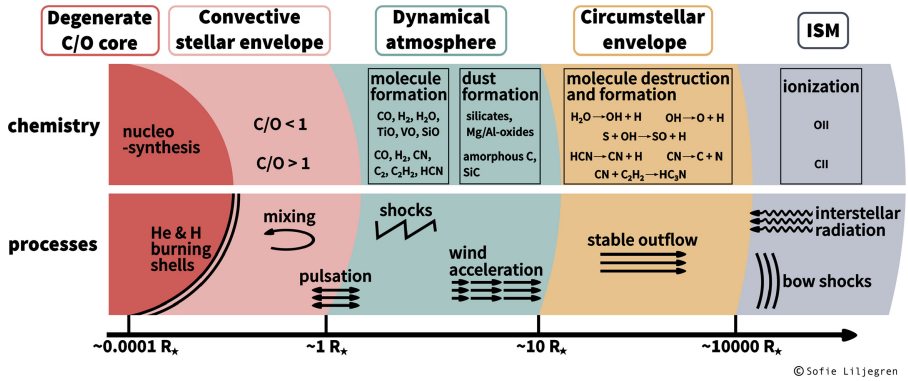

Figure 8.3. Schematic illustration of an AGB star and its circumstellar environment, including regions and processes discussed in the text. Boundaries between layers are indicated in units of stellar radius ($R_* \sim 1$ AU ~200 $R_\odot$ for a typical AGB star). Image credit: created by and courtesy of Sofie Liljegren; reproduced with permission from Astronomy and Astrophysics Review (Höfner & Olofsson 2018).

likely to decline monotonically with r. Simple molecules such as H_2, H_2O, CO, and SiO become stable, and dust forms as gas temperatures drop below the condensation temperatures of major solids ($T \lesssim 1500$ K). The grains are driven outward from the star by radiation pressure and transfer momentum to the gas by collisions. The number density of gas in the stellar wind also declines with r due to dilution, such

that $n \propto r^{-p}$, with $p = 2$ for uniform expansion at constant speed. The outer boundary of the circumstellar envelope may be considered as the radial distance $r \gtrsim 10^4 R_*$, at which temperatures and densities approach interstellar values. Dependent on the density of the local ISM and the star's relative motion, a significant bow shock may be produced (Cox et al. 2012).

Grain formation is expected to be most rapid near the transition zone from dynamical atmosphere to circumstellar envelope ($r \sim 10\ R_*$; Figure 8.3). Here, gas densities are typically $n \sim 10^{19}$ m^{-3}, orders of magnitude higher than those in even the densest interstellar clouds, and temperatures fall below the condensation temperatures of common refractory solids. This confluence of physical conditions ensures that the atmospheres of such stars are efficient producers of dust. The gaseous wind flowing into this zone contains a mix of atomic, ionic, and molecular gas in proportions that vary according to ambient conditions. Ionization inhibits nucleation, because positively charged particles repel each other, but the flux of ionizing radiation is expected to be minimal unless there is a significant contribution from the chromosphere or from a hot binary companion star. Pulsational instabilities inherent to these aging stars drive periodic variations in physical conditions and may induce cyclic phases of grain nucleation, growth and ejection (Gail et al. 2016; Bladh et al. 2019).

The formation of solid particles in a gas that undergoes cooling has been discussed in terms of classical nucleation theory (e.g., Salpeter 1974), originally formulated to describe the condensation of liquid droplets in the Earth's atmosphere. The theory assumes that the system maintains thermal equilibrium. Condensation of some species X occurs when its partial pressure in the gas exceeds the vapor pressure of X in the condensed phase, and is most efficient at temperatures appreciably below the nominal condensation temperature. An individual unit of X in the gas phase (a monomer) is a constituent atom or molecule. Random encounters between monomers lead to the formation of clusters; for equilibrium, the number density of clusters containing i monomers is

$$n_i = n_1 \exp(-\Delta E_i / kT) \tag{8.1}$$

where n_1 is the number density of individual monomers and ΔE_i is the thermodynamic free energy associated with the formation of the cluster. For small clusters, ΔE_i increases with i, and thus n_i decreases. Above some critical size, however, the addition of further monomers is energetically favorable; the clusters become stable and grow to a maximum size limited by the availability of monomers. Classical nucleation is thus a two-step process: (i) formation of clusters of critical size, and (ii) growth of clusters into macroscopic particles.

Classical nucleation theory is a useful starting point, but its applicability as a description of grain formation in stellar atmospheres must be addressed. Pressures in the nucleation zone of a red-giant wind are typically less than in the terrestrial atmosphere by at least a factor of 10^4. Thus, the timescale for nucleation to occur may be longer than the timescale in which the physical conditions undergo appreciable change, and condensation is not then an equilibrium process

(Donn & Nuth 1985). Furthermore, solid particles are typically held together by strong valence bonds rather than by the weak polarization forces that bind liquid droplets, and the formation of grains thus involves chemical reactions as well as physical clustering. Whereas classical theory describes the nucleation and growth of particles that are chemically identical to the original monomers, chemical reactions integral with the nucleation process may lead to the formation of solids (such as silicates) for which no equivalent monomer is available in the gas. Nevertheless, Paquette & Nuth (2011) conclude that the assumptions inherent in classical nucleation theory have only a second-order effect on the predicted size distribution and number density of grains forming in circumstellar outflows. See also Agúndez et al. (2020) for further discussion.

8.1.2 The C/O Ratio

The molecular chemistry of the gas in the nucleation zone of a stellar atmosphere is largely determined by a single parameter, the numerical abundance of C relative to O. The precise value of this ratio is crucial in determining the nature of the available monomers and hence the composition of the dust that grows from them. This condition arises from the fact that carbon monoxide, the most abundant of all molecules containing condensible elements, forms readily and remains stable in circumstellar gas at temperatures below about 3000 K. The binding energy of CO (11.1 eV) is sufficiently high that the bond is not readily broken in simple gas-phase reactions. Thus, despite its status as a radical, CO is chemically rather unreactive. Furthermore, CO cannot itself condense into solids in such environments. The abundance of CO in the gas is thus effectively limited, in most situations, only by the abundances of the constituent atoms: whichever element out of C and O is less abundant tends to remain sequestered in gaseous CO, and is therefore unavailable to form solids.

Stars that show observational evidence for circumstellar dust production (Section 8.2) may be divided into two broad categories, based on determinations of their atmospheric C/O ratios: those with C/O <1 (classified type M in the normal spectral sequence), and those with C/O >1 (carbon stars, type C). Carbon is produced by helium burning in stellar interiors during the course of their post-main-sequence evolution (Section 7.1.1), and enrichment of their atmospheres occurs when and if this product is dredged up to the surface by deep convection currents and pulsational instabilities (Figure 8.3). For stellar populations with metallicities similar to that of the Sun, the initial C/O ratio is about 0.5 (Table 7.1); in the atmospheres of carbon stars, it is enhanced typically to values in the range 1.0–1.5. The prediction of nucleation models, largely confirmed by observations, is that M-type stars produce only oxygen-rich dust and C-type stars produce only carbon-rich dust.

The distinction between these situations is not absolute, however. As a star evolves, it may undergo successive phases of mass loss that synchronize with periods of dredge-up, leading to time-dependent changes in the nature of its dust production. A transition occurs when C/O ~ 1 (examples are classified S-type) in which C and O effectively block each other from participation in grain formation. The efficiency of

dredge-up for any given star depends on its initial mass, composition, and subsequent mass-loss rate, and not all will ultimately acquire carbon-rich atmospheres. In a population of approximately solar metallicity, carbon stars tend to occupy a rather narrow range in mass (~1.5–3 $M_\odot$; e.g., Abia et al. 2020). Stars of lower mass are less likely to dredge up sufficient carbon; those of higher mass tend to consume it by C → N conversion, caused by CNO-cycle reactions in an H-burning shell.

8.1.3 Oxygen-rich Stars

Figure 8.4 illustrates the temperature-pressure (T, P) phase diagram for an atmosphere of solar composition (C/O ≈ 0.5). Gas streaming outward from the star follows a trajectory from upper right to lower left. The most abundant monomers that might participate in the production of solids as the gas cools are Fe, Mg, SiO, and H_2O (e.g., Gail & Sedlmayr 1986; Ferrarotti & Gail 2006; Gail et al. 2013). However, the first phase of grain formation involves rarer elements such as Al, Ca, and Ti, which form oxides such as alumina (Al_2O_3) and perovskite ($CaTiO_3$) at $T \sim 1500$ K. Although contributing little in terms of mass, these high-temperature condensates might facilitate the deposition of more abundant solids by providing nucleation centers (Onaka et al. 1989).

The major condensation phase begins as the temperature falls below about 1200 K, with the nucleation and growth of amorphous SiO clusters. The clusters chemisorb

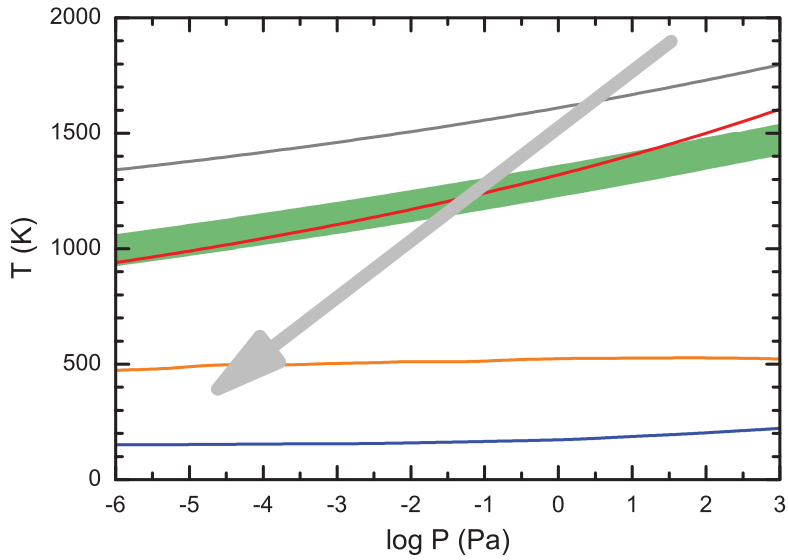

Figure 8.4. Temperature-pressure phase diagram illustrating stability limits of solids condensing in an atmosphere of solar composition. The gray arrow indicates the general trajectory of changing physical conditions in the outflow of a red giant. The green band corresponds to the zone in which magnesium silicates of mixed stoichiometries ($MgSiO_3$, Mg_2SiO_4) become stable. Other curves correspond to alumina (Al_2O_3, gray), metallic iron (red), wüstite (FeO, orange), and H_2O-ice (blue). Adapted from Salpeter (1977) with additional data from Barshay & Lewis (1976) and Gail et al. (2013).

other monomers, and abstraction of O from H_2O leads to further oxidization. Subsequent annealing may then result in the growth of linked SiO_3 chains with attached Mg cations (enstatite, $MgSiO_3$) or individual SiO_4 tetrahedra joined by cations (forsterite, Mg_2SiO_4). In an atmosphere of solar composition, one might expect silicates of mixed Mg/Fe content to dominate as thermodynamically favored end products, but a kinetically controlled formation process favors Mg silicates because they tend to form more rapidly, and there may be insufficient time to reach the most energetically favorable configuration (Nuth 1996; Rietmeijer et al. 1999). Iron might solidify as a pure metal, but laboratory simulations suggest that FeO monomers cluster more efficiently than Fe (Kimura et al. 2017). At $T \sim 700$ K, essentially all of the metallic elements are likely to have condensed into solids in some form or another. Finally, water-ice may condense in an optically-thick outflow at $T \lesssim 200$ K. A macroscopic grain emerging from such an atmosphere is thus likely to have a layered structure, dominated by Mg silicates, metallic iron and/or Fe oxides, perhaps deposited on a refractory "seed" nucleus, and coated with a thin surface layer of ice.

It is of interest to compare models for the condensation of solids in O-rich red giant winds with corresponding models for protoplanetary disks. Prevailing physical conditions may be similar, and in the case of the solar nebula the same mix of chemical elements is assumed, so the phase diagram in Figure 8.4 is relevant to both situations. It is therefore unsurprising that solids predicted to condense are broadly similar (e.g., Barshay & Lewis 1976; Lodders 2003). However, the dynamic evolution of the solar nebula was different, such that the condensation process may have been closer to thermodynamic equilibrium. Disparities in the composition and structure of the solids are therefore expected. Under equilibrium conditions, for example, FeO and H_2O may react with magnesium silicates at $\lesssim$400 K to form hydrated minerals such as serpentine, common constituents of primitive meteorites, whereas silicate dust in the ISM appears to be anhydrous (Section 5.2.1).

8.1.4 Carbon Stars

The equivalent phase diagram for a carbon-rich atmosphere is shown in Figure 8.5. A C/O ratio of 1.1 is assumed (the effect of varying C/O is also shown in the case of solid carbon). O is expected to be entirely sequestered into CO gas and therefore unavailable to form solids, as previously discussed. The first condensates to form in the cooling outflow are rare metallic carbides such as TiC (notable for their presence in presolar meteoritic stardust; Bernatowicz et al. 2005). However, unlike the situation in an O-rich atmosphere, chemical reactions involving metals do not regulate the primary phase of dust formation, which begins as temperatures drop below about 1500 K. Carbon itself is the dominant product (amorphous and graphitic forms have essentially the same stability limits). SiC particles may appear simultaneously or at somewhat lower temperatures, and metallic Fe solidifies at $T \sim 1200$ K. Iron carbide (Fe_3C) is also a potential product but is unlikely to be more than a trace constituent, its abundance limited by prior condensation of C.

The shape of the condensation curve for carbon is governed by the nature of the dominant monomer, which ranges from atomic and molecular carbon to

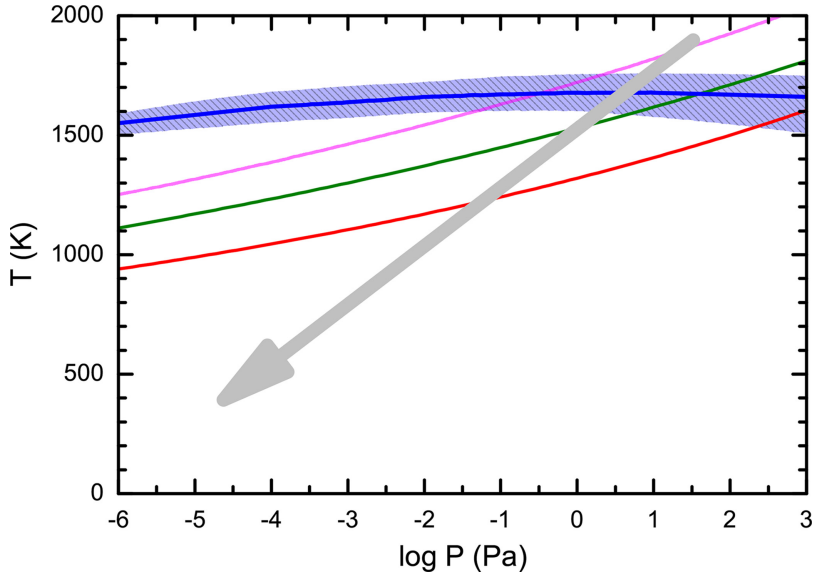

Figure 8.5. Similar to Figure 8.4 but for an atmosphere enriched in carbon, with solar abundances assumed for other elements. Colored curves correspond to graphitic carbon (blue), TiC (magenta), SiC (green), and metallic iron (red) for C/O =1.1. The blue shaded band illustrates the effect on carbon condensation of varying C/O from 1.05 (lower bound) to 1.2 (upper bound). Based on data from Lodders & Fegley (1995).

hydrogenated molecules such as C_2H_2 and CH_4, according to physical conditions and resultant chemical processes in the gas (Salpeter 1977). In the condensation zone of a red giant, acetylene (C_2H_2) is usually the dominant monomer. The kinetic processes that lead to the production of dust in this environment are analogous to soot production by combustion of hydrocarbons (Frenklach & Feigelson 1989; Tielens 2008), in which the products assemble into structures containing linked hexagonal rings. However, the molecular structure of the principal monomer is H–C≡C–H, the simplest example of a saturated *linear* molecule involving carbon bonding with alternate single and triple bonds. In order to construct aromatic hydrocarbons, the triple (sp) bond must be replaced by a double (sp^2) bond, a change that may result from a hydrogen abstraction reaction such as

$$C_2H_2 + H \rightarrow C_2H + H_2 \tag{8.2}$$

in which the product radical is structured C=CH, and is therefore effectively a ring segment (see, e.g., Figure 6.6). The ring may be closed by chemical reactions that attach two further monomers. Once formed, the ring is stable and can grow cyclically by abstraction of peripheral H atoms and attachment of further segments. This growth process may lead to the construction of planar PAH molecules containing multiple rings. However, competing reactions attach non-aromatic units to the rings. The likely outcome of the growth process is amorphous carbon, in which randomly-grouped ring clusters are connected by bridging units with linear (sp) or tetrahedral (sp^3) bonding (e.g., Santoro et al. 2020). This is, indeed, consistent

with the known properties of soot particles. Amorphous carbon lacks the long-range order found in crystalline forms with sp^2 (graphite) or sp^3 (diamond) bonding.

The nucleation process outlined above assumes that the atmosphere of the carbon star remains hydrogen-rich, as is usually the case. Rare exceptions include the R Coronae Borealis (RCB) class of variable stars, which are anomalously deficient in hydrogen for reasons that are not yet fully understood (Montiel et al. 2018). Dust is known to form rapidly in episodic bursts in the atmospheres of RCB stars, evidenced by dramatic dimming of their light curves attributed to a sudden onset of circumstellar extinction. Both the physics and the chemistry of grain formation are likely to diverge from those of typical carbon stars, nucleation occurring in regions closer to the photosphere and at significantly higher temperature, where no molecules are present in the gas (Whitney et al. 1993). C itself is then the only abundant monomer. The atoms may assemble into aromatic structures with unsaturated peripheral sites, forming amorphous carbon grains with low hydrogen content.

8.1.5 Planetary Nebulae

The core of a star on the asymptotic giant branch ultimately collapses to become a hot white dwarf, simultaneously ejecting its outer layers to form a planetary nebula (PN). The morphologies of these nebulae differ dramatically, ranging from classic rounded forms that inspired their moniker to bipolar structures such as that illustrated in Figure 8.1 (see Kwitter & Henry 2022 for a comprehensive review). The origin of this diversity is not fully understood, but may be attributed in part to differences in mass (stars that produce bipolar nebulae are typically more massive) or the influence of a binary companion (Kastner et al. 2018). Each example provides a snapshot of a brief (10,000 yr) period in a star's evolution, in which the dusty circumstellar outflow created during the AGB phase is illuminated by its newly-unveiled core. Mass loss rates increase with luminosity as the star ascends the AGB, formation of the PN preceded by a "superwind" phase in which gas and dust stream outward at speeds $\sim$10 km s^{-1}. As the outer layers of the star dissipate, the compact core is exposed. The surface temperature of the core may be as high as 100,000 K, generating an intense flux of high-energy photons that ionizes the expanding envelope. As previously noted, grain nucleation tends to be inhibited in ionized gas, and little or no new dust production is expected to occur in the planetary nebula itself. The expanding gas may be accelerated to speeds $\sim$100 km s^{-1}, an order of magnitude higher than earlier wind speeds. Material from previous phases of mass loss may thus be swept up and reprocessed (see Figure 8.1), and some grain materials may be destroyed. However, Stasinska & Szczerba (1999) argue that the timescale for grain destruction in planetary nebulae is longer than their lifetimes. In common with their precursors, PNe may be grouped according to C/O ratio, which corresponds to the nature of their observable dust content.

8.1.6 Core-collapse Supernovae

The progenitors of core-collapse supernovae are stars of initial mass $\gtrsim$8 $M_\odot$. They evolve to become supergiants after leaving the main sequence (Figure 8.2),

meanwhile maintaining hydrogen-rich photospheres, while the products of successive nuclear fusion cycles accumulate inside (Section 7.1.1). A supernova is triggered when internal accumulation of Fe reduces energy production to a point where the core undergoes gravitational collapse. The expanding remnants of these cataclysms are major sources of important dust-forming elements, most notably O, Mg, and Si (Johnson 2019). The extent to which these and other elements condense into solids prior to reaching the ISM has long been a topic of debate, but there is an accumulation of observational and experimental evidence, reviewed in the following sections, for significant dust formation in the ejecta. Progress toward the development of robust theoretical models for nucleation, growth and survival in this unique environment is discussed in a pair of review papers by Sarangi et al. (2018) and Micelotta et al. (2018), to which the reader is referred for detailed discussion. Some key points are summarized here.

As in other potential sources of circumstellar dust, a fundamental requirement is the presence of gas containing elements with an affinity for the solid phase under conditions of temperature and pressure that allow solids to nucleate and grow. In the wind of a red giant, such conditions may occur or recur on timescales of up to a million years; in a supernova they persist for less than a decade (Dwek et al. 2019). Dust is predicted to form in the cavity of hot gas that expands behind the initial blast wave caused by the explosion. Nucleation is inhibited by a flux of Compton electrons, energized by γ-ray photons released by decay of radioactive ^{56}Ni in the explosion, which ionizes and dissociates potential monomers. The cavity is also subject to disturbance by a reverse shock, arising from the impact of the blast wave on the outer layers of the progenitor and its circumstellar envelope (e.g., Bocchio et al. 2016). Depending on the composition and initial size of the condensates, processing by the reverse shock may lead to substantial ablation or even total destruction of the dust if it forms in a uniform outflow. However, the likely presence of denser clumps of gas in the outflow enhances rates of growth and provides a measure of protection. The shock wave decelerates as it propagates into a clump, thus greatly reducing rates of ablation.

Dust formation in supernovae is obviously not an equilibrium process. It may be simulated by application of chemical kinetics, considering evolving physical conditions in stratified layers of ejecta (Sarangi & Cherchneff 2013). The cycle begins with the formation of simple molecules such as CO and SiO. The ensuing chemistry is then dependent on the C/O ratio (Section 8.1.2). Core-collapse SNe are prolific sources of oxygen overall, but the degree of mixing with carbon varies from layer to layer, and dissociation of CO by Compton electrons may allow some C-rich dust production even in an O-rich gas (Clayton 2013; Liu et al. 2018). Potential monomers include many of those discussed in the context of red giant winds and, similarly, the condensates may range in composition from silicates and oxides to pure metals, sulfides, carbides, and carbon. Grains formed in this environment carry a memory of their origins, in the form of unique isotopic signatures, enabling identification of presolar examples in remnants of the Sun's protoplanetary disk (Section 8.3).

8.1.7 Exploding White Dwarfs

White dwarfs are the inert, degenerate cores of expired low and intermediate-mass stars. If left in isolation, they undergo no further thermonuclear activity that might exhume their heavy elements or kindle new production. In a close binary system, however, accretion of matter onto a white dwarf from a companion star may trigger such an event. If the white dwarf reaches a critical mass, it detonates as a type Ia supernova. Explosive nucleosynthesis then leads to copious production of Fe and other metals near the iron peak (Figure 7.2; see Johnson 2019). However, unlike core-collapse supernovae, type Ia events seem unlikely to be significant sources of dust: models suggest that grains either fail to condense or are subsequently destroyed by shocks (Dwek 2016; Kimura et al. 2017; Sarangi et al. 2018), consistent with a general lack of observational evidence for intrinsic dust in their expanding remnants (Section 8.2.1). The importance of type Ia SNe to dust production is the creation of relevant elements rather than dust itself. See also Section 7.3.4 for related discussion.

A distinct but related phenomenon is a nova outburst. This is caused by explosive thermonuclear ignition of matter accreting onto the outer layers of the white dwarf from its binary companion. In this case, however, the white dwarf maintains a subcritical mass and is not destroyed. The outburst ejects a rapidly expanding shell of ionized gas. Dust grains may begin to condense as the gas cools, evidenced by simultaneous occurrences of visual dimming and excess infrared emission some 30–100 days after the event (see Bode 2010 for a review). As before, grain formation is expected to commence when the expanding shell cools to temperatures $\lesssim$1200 K at which refractory solids composed of abundant elements become stable. Efficient dust production requires that the density is above some critical value at the condensation radius, and this depends on the total mass of ejected material. The availability of neutral atomic and molecular monomers is initially limited by UV radiation from the white dwarf, but the first condensates in a relatively dense flow will provide self-shielding if the dust becomes optically thick. Thus, some novae are copious sources of dust, while others produce little or none. Possible condensates include both oxygen-rich and carbon-rich compounds, ranging from silicates and SiC to hydrocarbons and solid carbon. However, as dust-producing novae are relatively rare events, they account for only a small proportion ($\sim$ 1%) of all stardust injected into the ISM (Gehrz et al. 1998).

8.2 Observations of Stardust

Observational techniques used to explore the nature and composition of dust grains in the circumstellar outflows of evolved stars are analogous to those used to study dust in the interstellar medium, described in previous chapters. The primary phenomena available for observation are infrared emission from heated dust, solid-state spectral emission and absorption features, and extinction of starlight. Models constrained by such observations are fairly successful in elucidating the physical properties of the particles and identifying at least some of the constituent materials. Important results are reviewed in this section. Complementary insights gained from analyses of presolar stardust in meteorites are reviewed in Section 8.3.

8.2.1 Infrared Continuum Emission

Infrared continuum emission greatly in excess of that expected from the Rayleigh–Jeans "tail" of a normal stellar photosphere is a defining characteristic of stars with circumstellar dust. Ultraviolet, visible, and near-infrared radiation from the photosphere is absorbed, and the heated grains emit at longer wavelengths. The spectral energy distribution (SED) of the emergent radiation depends on several factors, including the luminosity and spectrum of the star itself, the radial distribution of matter in the expanding envelope, and the composition and temperature of the dust. Radiative transfer models developed to simulate this emission are complex and dependent on numerous variables, but nonetheless important because they help to elucidate the dust formation process, the properties of the particles, and the mass-loss rates of the stars that produce them (e.g., Groenewegen 2012).

Information specific to the composition of the dust arises from both the general form of the SED and the presence of any distinct spectral features. In the idealized case of an isothermal dust shell of temperature $T_{\rm d}$, the radiative flux from the dust varies as $F_\lambda \propto Q_\lambda B_\lambda(T_{\rm d})$, where Q_λ is the grain emissivity and $B_\lambda(T_{\rm d})$ is the Planck function (Section 2.3.3). In reality, of course, $T_{\rm d}$ varies with radial distance in the shell, from the condensation temperature of the primary solid phase at its inner boundary to interstellar values as $r \rightarrow \infty$ (Section 8.1.1), resulting in a composite spectrum. At sufficiently long wavelengths, however, B_λ is described by the Rayleigh–Jeans approximation and the spectral shape converges to

$$F_\lambda \propto \lambda^{-(\beta+4)} \tag{8.3}$$

independent of $T_{\rm d}$. The spectral index of the emissivity, β, varies with the composition and crystallinity of the grains, as discussed in Section 2.3.4.

A wealth of observational data is available on which to test models for dust emission from post-main-sequence stars, both in the Milky Way and in local-group galaxies (e.g., Groenewegen 2012; Groenewegen & Sloan 2018 and references therein). Occasionally, emission may originate from ambient interstellar dust that happens to lie near the star, as appears to be the case for certain first-ascent red giants (Jura 1999); but dust shells around more evolved objects with $T_{\rm eff} \lesssim 3500$ K (Figure 8.2) are ubiquitous and evidently of circumstellar origin. The observed spectral energy distributions of stars with both O-rich and C-rich atmospheres can generally be explained by models that assume expanding shells in which dust of the appropriate composition condenses at temperatures $\lesssim$1500 K. Examples are shown in Figures 8.6 and 8.7. In each case, starlight is strongly attenuated by an optically-thick envelope resulting from extended periods of dust formation during the AGB phase of the star's evolution. Grains in the outflows of such stars appear to have predominantly (but not exclusively) amorphous structure, characterized in O-rich stars by the silicate spectral features, and in C-rich stars by emissivity indices $\beta \sim 1$, consistent with the predictions of kinetic chemical models (Donn & Nuth 1985; Paquette & Nuth 2011). Some oxygen-rich stars show spectral evidence for partial crystallization of silicates in the outflows, a topic further discussed in Section 8.2.2.

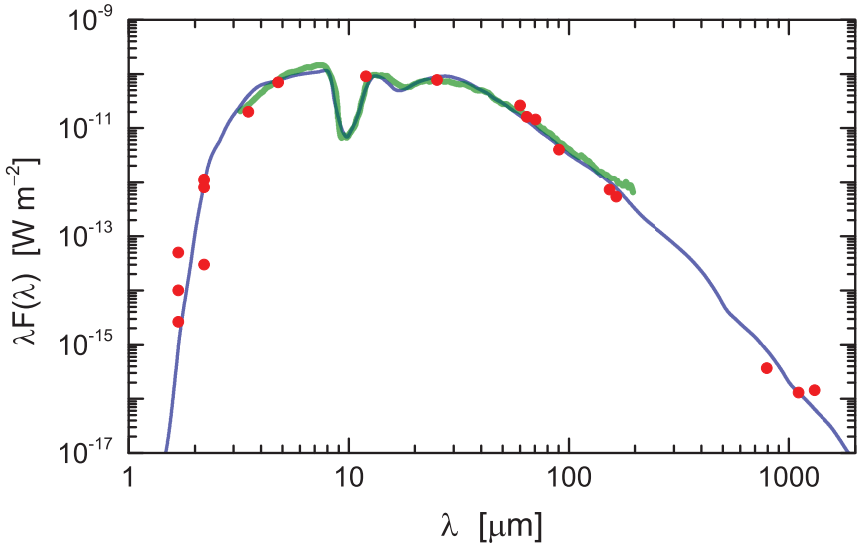

Figure 8.6. Spectral energy distribution of the oxygen-rich AGB star OH 26.5 + 0.6. Observational data include spectra from the short and long-wavelength spectrometers of the Infrared Space Observatory (green) and photometry from various sources compiled by Groenewegen (2012, red). Silicate features centered near 10 and 19 μm appear in absorption. The blue curve is a model based on calculations for olivine ($MgFeSiO_4$) particles of radius $a = 0.2$ μm (see Groenewegen 2012 for further details).

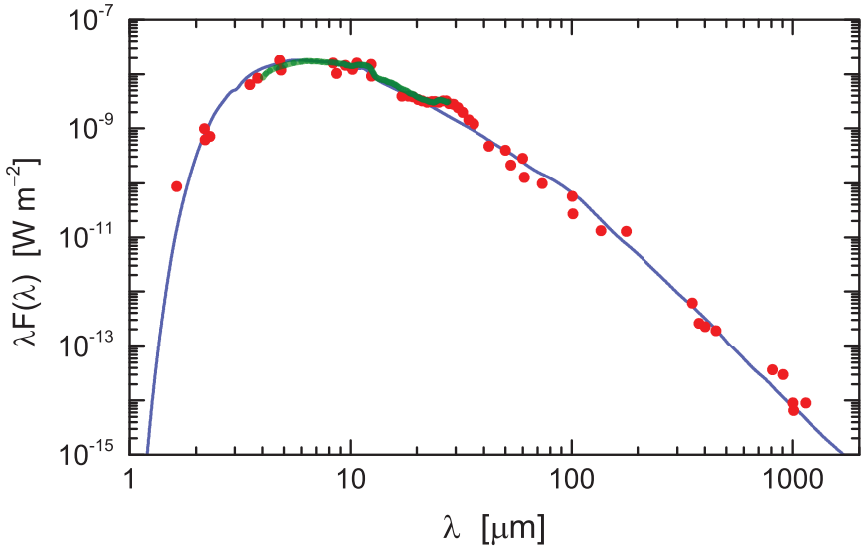

Figure 8.7. Similar to Figure 8.6 but for the carbon star IRC +10 216. The data include spectra from the Infrared Space Observatory (green curve; Thompson et al. 2006) and photometry (red circles), the latter corresponding approximately to the maximum phase of the star's variability. The model (blue curve) assumes amorphous carbon grains of radius $a = 0.16$ μm with a 3% admixture of SiC (Groenewegen 1997). See also Guélin et al. (2018) for further studies of IRC +10 216 and its environment.

The dust responsible for infrared emission from AGB stars such as those illustrated in Figures 8.6 and 8.7 is almost always unambiguously circumstellar in origin, but the situation for supernovae is more complex. The precursors of core-collapse SNe, the most important probable sources of supernova stardust (Section 8.1.6), evolve very rapidly and often detonate in relatively dense regions of the ISM, having had insufficient time to migrate far from their birth sites. Care must therefore be taken to distinguish between radiation emanating from dust created in the explosion and from pre-existing interstellar or circumstellar dust close to the source. Serendipitously, SN 1987A, the most closely studied of all core-collapse supernova to date, detonated in a low-density region of the Large Magellanic Cloud, in a line of sight clear of significant local or foreground extinction.

Evidence for dust formation in the ejecta of SN 1987A first appeared some 500 days after detonation. A systematic increase in mid-infrared flux was observed, consistent with the presence of grains of temperature $T_d \sim 600$ K (Wooden et al. 1993 and references therein). This was accompanied by an apparently simultaneous onset of a decline in visible light, steeper than the predicted rate of decay for the SN type, attributed to extinction. Subsequent monitoring of the infrared spectrum has shown a gradual cooling of the dust, evidenced by a shift of the peak toward longer wavelengths; by 2010 the dust temperature was approaching interstellar values ($T_d \sim 20$ K; Matsuura et al. 2011; Cigan et al. 2019; see Figure 8.8).

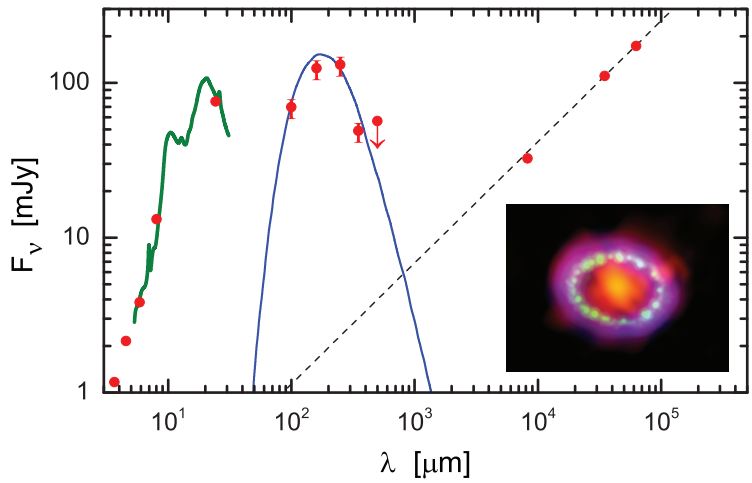

Figure 8.8. Spectral energy distribution of Supernova 1987A, based on infrared, submillimeter and radio data collected between 6000 and 9000 days after detonation (Matsuura et al. 2011 and references therein). The green curve is a spectrum from the Spitzer Space Telescope; red circles are photometric data from the Spitzer and Herschel Space Telescopes and ground-based observations. The blue curve is a dust model ($T_d \approx 20$ K) fitted to the far-infrared data. The dashed line represents synchrotron emission from hot ionized gas. A contemporaneous image is also shown, superposing data at submillimeter, visible and X-ray wavelengths (color-coded red, green, and blue, respectively). Image credits: ALMA (ESO/NAOJ/NRAO/A. Angelich); Hubble Space Telescope (NASA/ESA/R. Kirshner and P. Challis/Harvard-Smithsonian Center for Astrophysics/Gordon and Betty Moore Foundation); Chandra X-ray Observatory (NASA/CXC/Penn State/K. Frank).

Meanwhile, as dust internal to the expanding shock gradually cooled, evidence emerged for a spatially distinct reservoir in its path. This equatorial ring of circumstellar material around SN 1987A (Figure 8.8, inset image) is presumed to be a product of mass-loss during an earlier phase of the progenitor's evolution. First illuminated by the ultraviolet flash from the explosion, it was subsequently energized by the arrival of the shock, causing it to brighten across the spectrum. Shocked gas in the ring is a source of both X-ray and radio synchrotron radiation, its bead-like structure attributed to clumping. Mid-infrared radiation peaking near 20 μm in the SED (green curve in Figure 8.8) emanates from circumstellar dust in the ring, its spectral profile consistent with emission from silicate particles of temperature $T_d \sim 180$ K (Bouchet et al. 2006; Arendt et al. 2016). Dust in this hostile environment is gradually being decimated by sputtering; its estimated total mass ($\sim 3 \times 10^{-6}$ $M_\odot$) is minuscule compared with that of new dust formed behind the shock (red central area of the inset image), which has a probable range of 0.2–0.7 $M_\odot$ (Cigan et al. 2019).

Studies of recent historical supernovae in our Galaxy paint a somewhat consistent picture. Of these, SN 1572 (Tycho) and SN 1604 (Kepler) are classified type Ia (see Section 8.1.7), expected on theoretical grounds to produce little or no intrinsic dust, and observations of dust emission in their remnants can be explained entirely by ambient interstellar or circumstellar matter (Douvion et al. 2001; Williams et al. 2012). SN 1054 (progenitor of the Crab Nebula) is considered to be a core-collapse supernova, albeit with a relatively low estimated mass ($\sim$ 8–10 $M_\odot$), roughly half that of the SN 1987A progenitor. The estimated mass of dust attributed to condensation in SN 1054 is also relatively small, no more than about 0.05 $M_\odot$ (De Looze et al. 2019). Cassiopeia A is likewise considered to be the remnant of a core-collapse SN (its eruption date unknown, estimated circa 1680). It is located at a distance of $\sim$ 3.4 kpc in a direction close to the galactic disk, thus the line of sight contains copious quantities of interstellar matter, and this adds to the challenge of identifying dust intrinsic to the remnant. Detailed analyses of spatially-resolved infrared and submillimeter data reveal concentrations of cold dust in the unshocked ejecta of Cassiopeia A with an estimated total mass in the range 0.3–0.6 $M_\odot$ (De Looze et al. 2017), comparable with that of SN 1987A.

8.2.2 Infrared Spectral Features

Infrared spectroscopy provides a potentially powerful and direct means of identifying grain constituents in stellar ejecta, as previously discussed in the context of interstellar particles (Chapter 5 and Section 6.2). The principal features attributed to circumstellar dust and PAHs are listed in Table 8.1. Various subsets of the listed features are commonly observed in red supergiant (RSG) and asymptotic giant branch (AGB) stars, and in planetary nebulae (PNe). In contrast, there is little evidence to date for spectral features that can be attributed to intrinsic dust in supernovae. Silicate emission was detected from the shocked circumstellar ring of SN 1987A (the spectrum in Figure 8.8 exhibits 9.7 and 19 μm peaks on a steeply-rising continuum) but not in the central condensation zone when it was warm

Table 8.1. Infrared Circumstellar Dust Features of Evolved Stars and Planetary Nebulae

Wavelengths (μm)	Carrier	a/e?	ISM?	Object Types
Oxygen-rich:				
9.7, 19	a-silicates	a/e	Yes	RSG, AGB, PNe
10.0, 11.2, 16.3, 19.5, 23.5, 27.5, 33.5	c-forsterite	e	No?	RSG, AGB
10–17	a-Al_2O_3?	a/e	No	RSG, AGB
13	c-Al_2O_3?	e	No	RSG, AGB
20	FeO? MgO?	e	No	RSG, AGB
3.1, 6.0, 11.5	H_2O ice	a	Yes	OH/IR stars
44, 62	H_2O ice	e	No	OH/IR stars
Carbon-rich:				
3.3, 6.2, 7.7, 8.6, 11.3, 12.7	PAHs	e	Yes	PNe
11.2	SiC	a/e	No	AGB, PNe
21	?	e	No	PNe
30	MgS?	e	No	AGB, PNe

Notes: Features are grouped by the C/O ratio of the source. "PNe" here includes both planetary nebulae and their immediate precursors (post-AGB stars, proto-PNe). Only the principal features of PAHs and a typical crystalline silicate (c-forsterite) are listed. Information is included on whether each feature is generally seen in absorption or emission and whether it has a known interstellar counterpart. Note that a small subset of C-rich objects also display silicate features.

enough to be observable in the mid-infrared (Wooden et al. 1993). This situation might be interpreted as evidence that supernova dust is generally featureless (e.g., pure carbon or metallic iron rather than silicates), but it might also arise from masking of emission features by self-absorption in optically-thick ejecta (Dwek & Arendt 2015). Moreover, at least one core-collapse supernova has been observed to develop a silicate signature at the expected epoch of dust condensation (Kotak et al. 2009). Large quantities of elemental Mg and Si are generated in these events, and observations indicate that they become increasingly depleted from the gas, strengthening the case for silicates as primary condensates in the ejecta (Dwek et al. 2019).

The sources most widely observed to show circumstellar dust signatures are AGB stars and the planetary nebulae that they engender. Features may appear in net emission or net absorption, dependent on the radiative environment, the temperature and density profiles of the envelope, and the optical properties of the dust, factors that vary with the evolutionary state of the source. AGB stars exhibit distinctive infrared spectra governed by their atmospheric C/O ratios (Section 8.1.2), as illustrated in Figures 8.6 and 8.7. OH 26.5 + 0.6 belongs to the OH/IR subgroup of O-rich AGB stars undergoing rapid mass-loss (Section A.3), generating an optically-thick circumstellar shell rich in silicates (Justtanont et al. 1996); IRC +10 216 is a carbon star in an otherwise analogous evolutionary phase. Their SEDs differ most clearly in the mid-infrared, with silicates detected only in the former.

Extracting precise information from the spectra on the composition of the dust is challenging for several reasons. The observed SED may be modeled as a combination of distinct stellar and circumstellar components, after correcting for foreground

extinction. The stellar component typically varies systematically with time, so ideally observations from different instruments and at different wavelengths should be matched to the same phase of the light curve. Broad gas-phase molecular bands that resemble solid-state features may be present in the spectrum; however, these are generally most prominent at wavelengths below 8 μm, whereas the dust features lie mostly between 8 and 30 μm. The circumstellar component may include a superposition of absorption and emission features arising in different regions along the line of sight. The opacity of the envelope increases as dust accumulates, and if it becomes optically thick the stellar photosphere is hidden from view. Simultaneously, the dust from which we receive most radiation becomes cooler, and absorption in the spectral features increases relative to emission. With all these factors taken into account, it is possible to deduce realistic spectral models that elucidate the composition of the dust, although some features still lack secure identifications. See Messenger et al. (2013), Golriz et al. (2014) and Shepard & Speck (2021) for related discussion.

Silicate features are invariably prominent in the spectra of dusty oxygen-rich stars. In some cases, the profiles of the 9.7 μm and 19 μm features are smooth and distinct, resembling those seen in the ISM, as expected if amorphous, Mg-bearing silicates are the primary constituents of the dust. Indeed, the circumstellar 9.7 μm feature observed in emission toward the red supergiant μ Cephei (Section 6.2.1) has been used as a standard reference profile in models fitted to its interstellar counterpart in absorption. In other cases, the spectra are more complex, signaling differences in silicate mineralogy and/or additional contributions from other compounds. Observed source-to-source variations in the spectra provide a basis for classification schemes that characterize the evolutionary state of the envelope and constrain the chemical and mineralogical properties of the dust (Begemann et al. 1997; Sloan & Price 1998). Representative examples from a study by Golriz et al. (2014) of AGB stars with silicate features in emission are shown in Figure 8.9 (upper frame). Spectra based on laboratory data of some candidate materials are also shown.

The silicate-dominated spectra present several interpretative challenges. One notable issue is the emissivity (or opacity) of the dust in the spectral range between the principal Si–O stretching and bending modes ($12 < \lambda < 16$ μm), which typically exceeds levels consistent with silicates alone, either amorphous or crystalline. A plausible explanation is the expected presence of aluminum in the particles. This highly condensible element (Section 7.2.3) is among the first to solidify in a cooling atmosphere. Its predicted initial form in an O-rich outflow (Section 8.1.3) is the refractory oxide alumina (Al_2O_3); some might also be incorporated into aluminosilicates (Mutschke et al. 1998) or spinel ($MgAl_2O_4$; DePew et al. 2006). The spectral profile of amorphous Al_2O_3 (Figure 8.9) peaks near 12 μm, where it blends with the silicate stretching mode and adds opacity between the two principal features. Furthermore, in its *crystalline* mineral form (corundum), Al_2O_3 produces a sharper, narrower feature centered near 13 μm, providing a tentative identification of a dust feature at this wavelength seen in many O-rich AGB stars, including one of those shown in Figure 8.9 (blue curve); see Begemann et al. (1997), Sloan et al. (2003) and Golriz et al. (2014) for further discussion and examples. Other metal oxides that may

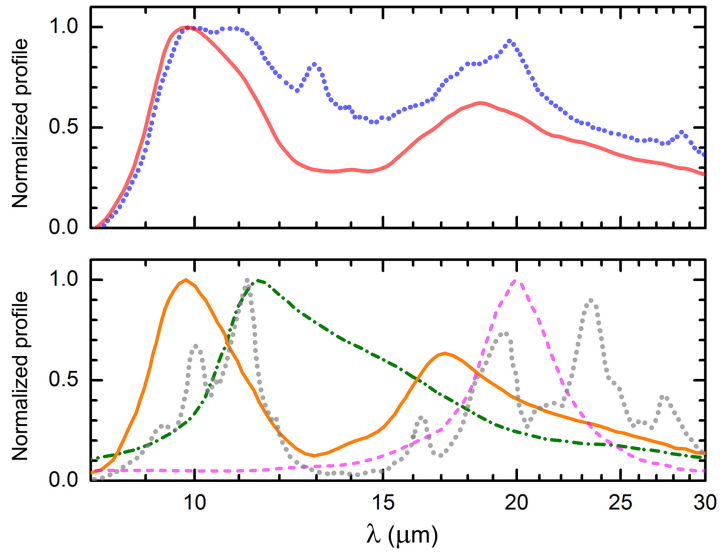

Figure 8.9. Contrasting dust emission features in two oxygen-rich AGB stars, compared with data for some candidate materials. Upper frame: spectral profiles of c32-16 (solid red) and NGC 6522-5 (dotted blue), from the analysis by Golriz et al. (2014) of observations obtained by the Spitzer Space Telescope. Lower frame: synthetic spectra based on the optical properties of amorphous olivine ($MgFeSiO_4$, solid orange, Dorschner et al. 1995), crystalline forsterite (Mg_2SiO_4, dotted gray, Jäger et al. 1998), amorphous alumina (Al_2O_3, dotted–dashed green, Begemann et al. 1997), and wüstite (FeO, dashed magenta, Henning et al. 1995). Each curve is normalized to unity at peak.

contribute to the observed profiles include FeO and MgO (Henning et al. 1995; Posch et al. 2002), both of which have features peaking near 20 μm; thus, if present, they overlap the silicate bending mode.

Spectral signatures of crystallization provide evidence for annealing of dust in the outflows. Laboratory data show that annealing of silicates causes dramatic changes in their spectra, sharpening the principal features and introducing distinct structure associated with various vibrational resonances in the lattice (Jäger et al. 1998; Fabian et al. 2000). The spectra differ in detail according to the specific composition and mineralogy of the silicate: results for crystalline forsterite are used here for illustration (Figure 8.9 and Table 8.1). Incorporating the data into spectral models is challenging, in part because the profiles are sensitive to grain size, shape and temperature as well as mineralogy, and it can therefore be difficult to constrain the mass ratio of crystalline to amorphous silicates in a given source by modeling its SED. Those with simple, smooth spectra (e.g., red curve in Figure 8.9) are clearly dominated by amorphous silicates, but the converse is not necessarily true. Even stars with complex spectra often lack diagnostic features in the 21–28 μm range that would be indicative of crystalline silicates (e.g., blue curve in Figure 8.9; more examples in Golriz et al. 2014), perhaps in some cases due to self-absorption (Jones et al. 2012). Others show clear evidence of crystallization (e.g., review by Henning 2010). It has been suggested that the degree of crystallinity may depend on the

mass-loss rate of the star, but this has not been confirmed: see Speck et al. (2008), Jones et al. (2012) and Liu et al. (2017) for further discussion.

Ice may form at sufficiently low temperatures in the outer envelopes of some O-rich stars (Section 8.1.3). The conditions needed for this to occur are most likely to arise during late phases of AGB evolution, as the mass-loss rate increases and the circumstellar envelope becomes optically thick: prime candidates are the OH/IR stars, distinguished observationally by OH maser line emission at radio wavelengths and continuum emission from cold dust in the infrared, with silicate features in absorption (e.g., Figure 8.6). The outer layers of the envelope are shielded from photospheric radiation, and a steep temperature gradient is established. H_2O molecules in the gas may then freeze onto the surfaces of refractory grains that formed previously in a hotter region of the outflow. Spectral features identified with H_2O-ice (Table 8.1) include the O–H stretching, bending and libration modes in absorption, and lower-energy lattice modes in emission (Boogert et al. 2015 and references therein).

It is informative to compare ice features observed in circumstellar outflows with those in interstellar environments. Examples are shown in Figure 8.10 of the absorption centered near 3.1 μm, identified with the O–H stretching mode of H_2O-ice, in the circumstellar envelope of OH 231.8+4.2 and in a prototypical molecular cloud. The profile observed in the OH/IR star is consistent with a model based on *pure* H_2O-ice mantles deposited onto silicate cores at a temperature of 80 K. Thus, as expected, they appear to be forming in substantially warmer conditions compared with ices in molecular clouds. Another difference is that the circumstellar ices are likely to be condensates of preformed gaseous H_2O monomers rather than the products of reactions between constituent atoms on grain surfaces (see Section 9.2.2). The circumstellar ice is

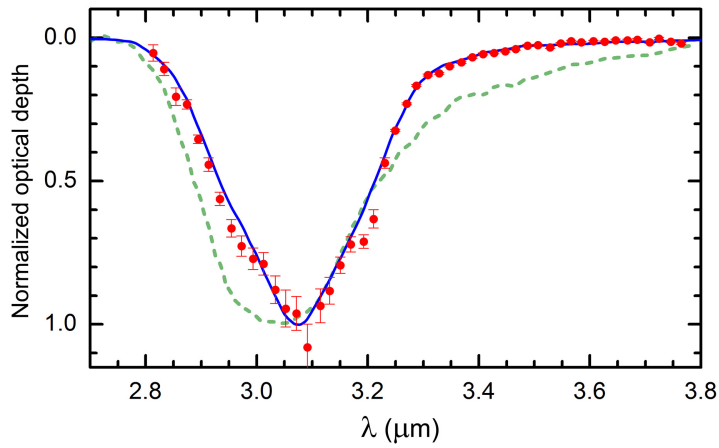

Figure 8.10. Circumstellar absorption centered at 3.1 μm toward OH 231.8+4.2 (red points), attributed to freeze-out of H_2O in its ejecta. The blue curve is a model fitted to the observed profile, assuming spherical grains consisting of H_2O-ice mantles of temperature 77 K and maximum radius 0.6 μm deposited onto silicate cores of radius 0.1 μm (Smith et al. 1988). Also shown for comparison is the profile of the interstellar ice feature observed in the Taurus dark cloud toward Elias 16 (green dashed curve: see also Figure 5.12).

at least partially crystalline, as confirmed by studies of its features at longer wavelengths (Boogert et al. 2015). Significantly, the circumstellar 3.1 μm profile lacks the extended long-wavelength wing characteristic of its interstellar and protostellar counterparts (Section 5.3.3). This difference might be compositional, or it might reflect a disparity in grain size. Circumstellar ice may be purer than interstellar ice, lacking additional absorbers such as ammonium hydrates and hydrocarbons that add opacity in the 3.2–3.6 μm spectral range; indeed, no carbon-bearing condensates are predicted in an oxygen-rich outflow (Section 8.1.2). A maximum radius $a \approx 0.6$ μm is suggested for ice-mantled grains toward OH 231.8+4.2 (Figure 8.10); those in dense molecular clouds may grow significantly larger, causing enhanced extinction by scattering that might account for the long-wavelength wing.

In contrast, the primary condensate in a C-rich outflow—carbon itself—is largely featureless in the infrared. Potential exceptions include lattice resonances in graphite (Draine 1984, 2016), but the predict features at 6.3 and 11.5 μm are very weak and have so far eluded detection. In any case, both condensation theory (Section 8.1.4) and radiative transfer models (Martin & Rogers 1987; Groenewegen 2012) suggest a preponderance of amorphous carbon over graphite. Vibrational modes in hydrocarbons are further candidates for detection, but cool stars do not emit sufficient UV flux to "pump" the familiar PAH emission spectrum (Section 6.2.2), and larger particles seem likely to have low hydrogen content (Chiar et al. 2013). Indeed, the only widely-observed circumstellar dust signature in cool carbon stars that lays claim to a secure identification is that of SiC near 11 μm (Table 8.1). This feature is most commonly seen in emission, but cases of its occurrence in net absorption have also been reported (Speck et al. 2009). An example of each is shown in Figure 8.11.

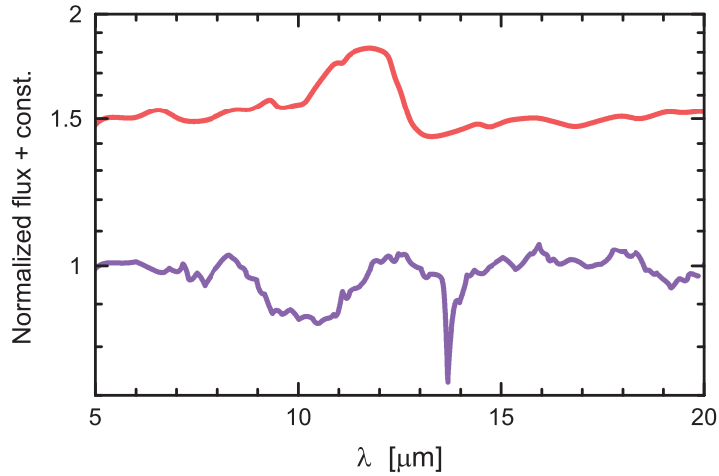

Figure 8.11. Dust features near 11 μm attributed to SiC in carbon stars IRC +10 216 (above) and IRAS 21318 +5631 (below). Each curve is the ratio of observed spectrum to fitted continuum (the upper curve displaced for display). The narrow 13.7 μm absorption in IRAS 21318+5631 is attributed to gas-phase C_2H_2. Based on spectra from the ISO archive analyzed by Thompson et al. (2006), Speck et al. (2009) and Messenger et al. (2013).

Detection of SiC in carbon stars is qualitatively consistent with condensation models for C-rich atmospheres (Section 8.1.4). However, extracting quantitative information on the nature and abundance of SiC in stardust from the observations is challenging for several reasons. Laboratory studies show that the position, width, strength and profile of the 11 μm feature are highly sensitive to the precise properties of the particles, including size, shape, purity and crystallinity (Mutschke et al. 1999). Condensation zones for SiC and solid carbon are partially overlapping in the phase diagram (Figure 8.5), so SiC-bearing particles in the outflows might assume structures ranging from pure SiC crystals to SiC seed particles coated with carbon or irregular mixtures of both materials. Thus, variations in physical conditions in the condensation zone may affect the structure of the particles produced, both from one source to another and over time in a specific source. In cases affected by self-absorption, the emitting grains may differ from the absorbing grains, not only in temperature but potentially in other ways that influence the profile, such as structure, purity, and size distribution. These factors may account for source-to-source differences in the position and width of the 11 μm feature, notably in the shift from net emission to net absorption (Figure 8.11). Because of such concerns, estimates of the mass ratio of SiC to generic carbon dust in stellar ejecta are uncertain. Results based on observations of stars in the Milky Way with approximately solar metal abundances typically range from 5% to 15% (Groenewegen et al. 1998), significantly lower than the predictions of AGB models constructed by Nanni et al. (2013).

As a star reaches the end of the AGB phase of its evolution, it sheds its outer layers to form a planetary nebula (Section 8.1.5). During the transition period, lasting perhaps a few thousand years, the color temperature of the stellar spectrum becomes progressively hotter as the core is gradually unveiled. Once the metamorphosis is complete, the circumstellar environment is exposed to intense, hard UV radiation emanating from the $T \gtrsim 50{,}000$ K core, now revealed as a white dwarf. The dramatic change in visual appearance is accompanied by corresponding changes in the spectrum. In carbon-rich objects, a signature development is the appearance of the PAH emission spectrum (Figure 8.12; see also Figure 6.7). Of course, the presence of PAHs in this environment is no surprise—their production is implicated in the growth of larger particles (Section 8.1.4). PAHs are not generally detectable in absorption in optically-thick circumstellar envelopes, the opacity arising in much larger grains; but on exposure to photons sufficiently energetic to induce thermal transients, free-flying PAHs immediately reveal their presence. See Section 6.2.2 for related discussion.

In addition to the PAH spectrum, Figure 8.12 exhibits emission features peaking at longer wavelengths that have proved difficult to identify. Of these, the broad band centered near 30 μm seems to be a common signature of stardust in C-rich environments, observed in AGB stars (see, e.g., Figure 8.7) as well as transition objects and PNe. An identification with MgS has been proposed but this is not well-supported by available evidence (see Messenger et al. 2013 and Zhang 2020 for detailed discussion). Its extreme width and star-to-star variations in shape suggest that the 30 μm "feature" is in fact a blend (Hrivnak et al. 2000), potentially with multiple carriers: Mishra et al. (2015, 2016) use two or three distinct Drude functions

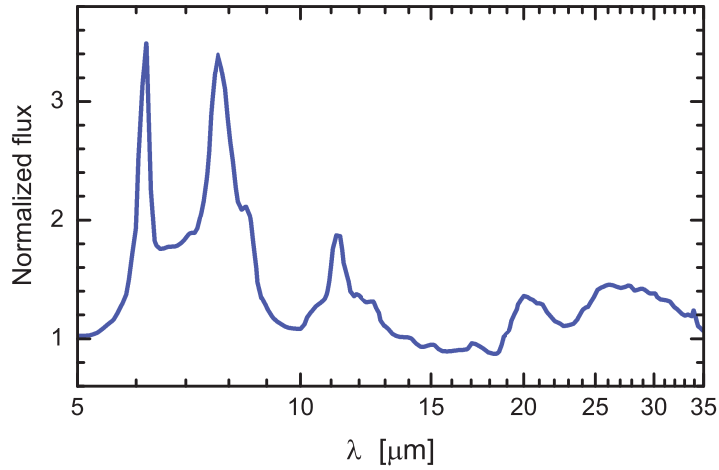

Figure 8.12. Circumstellar emission features toward IRAS 14429−4539, an example of a carbon-rich post-AGB star in the brief transitional period during which it evolves to become a white dwarf with a planetary nebula. The vertical axis is the ratio of observed flux to continuum fit from an analysis of archival ISO data by Mishra et al. (2016). The spectrum exhibits PAH features and unidentified peaks centered near 21 and 30 μm.

to model the observed profiles. Another unidentified feature, centered near 21 μm, is prominent *only* in the spectra of C-rich sources in transition between AGB and PN phases, where stellar color temperatures are intermediate between those of red giants and hot white dwarfs. Perhaps, in common with the PAH features, the carrier requires UV excitation to be observable, but is subsequently destroyed when the radiation field becomes too harsh.

As previously noted, not all carbon-rich sources display exclusively carbonaceous dust features: a small subset exhibits silicate emission features in their circumstellar envelopes (Little-Marenin 1986; Willems & de Jong 1986; Waters et al. 1998; Kwon & Suh 2014). It seems unlikely that these objects are true exceptions to the premise described in Section 8.1.2, which predicts that the gas-phase C/O ratio in the condensation zone controls the chemistry of dust production. In a single star, this ratio changes with time if the stellar atmosphere becomes carbon-enriched during successive episodes of dredge-up. Enrichment is associated with thermal pulses that induce temporary phases of rapid mass-loss (Zijlstra et al. 1992). The switch from O-rich to C-rich chemistry may therefore occur quite rapidly, creating a source of carbonaceous dust within an expanding envelope of silicate dust from earlier cycles of production. However, the expanding shells are expected to cool on timescales much shorter than the thermal pulse cycle (10^3–10^4 years; Iben & Renzini 1983), and it is then difficult to understand why the silicate features are observed in *emission*. But if the mass-losing star is a member of a binary system, its ejecta may be captured into the circumstellar envelope of the companion, which could then act as a reservoir of warm silicate dust formed at an earlier epoch. A further albeit less probable scenario is that both members of a binary system could be dust producers, one carbon-enriched, the other not.

8.2.3 Circumstellar Extinction

One important result arising from extinction by circumstellar dust has already been noted: an increase in infrared flux from the ejecta of certain stellar cataclysms (novae, core-collapse supernovae) may be accompanied by simultaneous dimming of the visible light, attributed to extinction, thereby providing corroborative evidence for the onset of dust formation. If the wavelength-dependence of the extinction can be measured, it may provide further insight into the nature of the dust. A specific question that can be addressed by such observations is the relationship between carbonaceous stardust and the absorber responsible for the interstellar UV extinction "bump" (Section 3.4), widely attributed to graphitic nanoparticles. Do the carrier particles (or their precursors) originate in stellar outflows?

A practical problem that constrains observing campaigns designed to address this question is the simple fact that most dust-producing stars are insignificant sources of ultraviolet radiation. This property is intrinsic to low-temperature photospheres, exacerbated by high extinction if the circumstellar envelopes are not optically thin. Because of this, only a small (and perhaps unrepresentative) subset of sources are feasible targets, specifically post-AGB stars (Figure 8.2) and members of the rare RCB class of eruptive variables. Observations designed to measure extinction in these objects were enabled by space telescope missions, most notably the International Ultraviolet Explorer, which was operational from 1978 to 1996 (little further progress seems to have been made since then). Extinction curves may be generated by methods analogous to those applied to studies of the ISM (Section 3.1), using either a model stellar atmosphere or observations of an unreddened star of matching spectral type as the basis for comparison. These methods are generally less reliable for studies of circumstellar extinction, however, as the targets typically have complex, non-standard photospheric spectra and are intrinsically variable. Care must also be taken to separate circumstellar and interstellar components of the measured extinction. However, if stellar variability results primarily from varying degrees of circumstellar extinction, as is generally the case for RCB-type stars, a comparison between spectra measured at bright and faint phases of the light curve may provide an extinction curve without reference to another object or model atmosphere, subject only to matching the stellar pulsational phase at high and low obscuration (e.g., Hecht et al. 1984). In serendipitous cases where a normal early-type star lies within or behind the circumstellar envelope of a dust-forming star, the former may be used as a probe of the extinction in the latter using the standard technique (e.g., Snow et al. 1987).

Examples of circumstellar UV extinction curves are illustrated in Figure 8.13 (displayed as extinction versus wavenumber, the conventional format for interstellar studies; Chapter 3). A broad peak centered near 4 μm^{-1} is evident in two of the three sources (see Hecht et al. 1984, Buss et al. 1989, and Drilling et al. 1997 for further examples). The mean wavelength of the peak is 240 ± 2 nm (Muci et al. 1994), substantially longer than that of the 217 nm interstellar feature. Both RY Sgr (an RCB-type star) and Abell 30 (a planetary nebula) are carbon-rich and hydrogen-deficient,

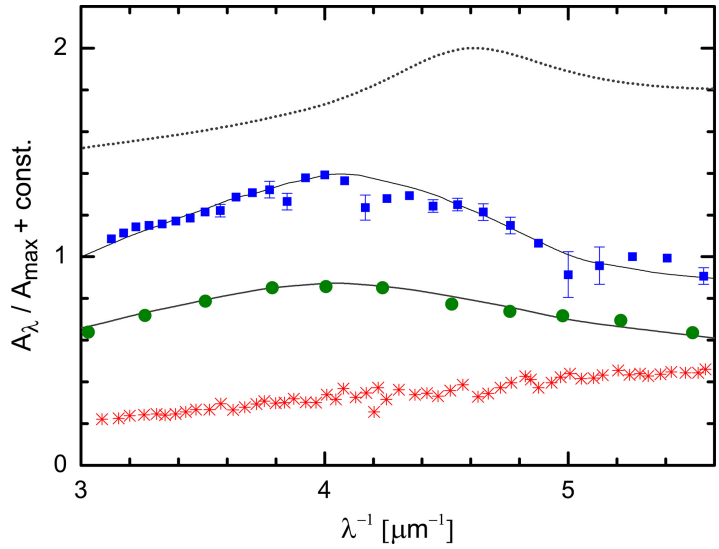

Figure 8.13. Examples of circumstellar ultraviolet extinction curves, compared with the mean for the diffuse ISM (dotted curve; Section 3.2.1). Vertical placement is arbitrary for display. RY Sgr (an RCB star, blue squares) and Abell 30 (a planetary nebula, green circles) both exhibit a broad absorption peak centered near 4 μm^{-1}, consistent with predicted profiles for absorption by sub-micrometer-sized amorphous carbon grains (solid curves). Extinction toward HR 4049 (also known as HD 89353, a post-AGB star, red asterisks) appears to be featureless. Based on data from Muci et al. (1994) and references therein.

as are other objects in which the 240 nm feature is detected. The most probable dust condensate in such an environment is amorphous or partially annealed carbon with low hydrogen content, and indeed the profile of the feature is well-matched by numerical models and laboratory simulations based on such particles (Hecht et al. 1984; Hecht 1991; Muci et al. 1994; Drilling et al. 1997). Grain radii yielding good fits are typically $a \sim 0.03$ μm, larger than those used to fit the interstellar feature (Figure 3.11). In contrast, the circumstellar UV extinction toward HR 4049 appears to be featureless (Figure 8.13, red). This carbon-rich post-AGB star may be atypical: it is a member of a close binary system with a circumbinary disk, in which the companion exerts a major influence on the physical and chemical evolution of the system (Malek & Cami 2014). Unlike stars that exhibit 240 nm features, HR 4049 is not depleted in hydrogen, a factor that suggests a plausible explanation: hydrogenation tends to suppress UV features in graphitic or amorphous carbon by localizing the electrons responsible for absorption (Hecht 1986).

The majority of stars for which circumstellar extinction curves have been studied are C-rich, but a few O-rich supergiants have also been investigated (Snow et al. 1987; Buss & Snow 1988; Seab & Snow 1989). To within the limits of the data, there is no evidence for either a mid-UV bump or a far-UV rise. The absence of an absorption feature is, of course, expected as dust forming in an O-rich environment should lack a carbonaceous component. In the best-studied case (α Sco), the extinction declines steadily with increasing wavenumber in the UV: the data are consistent with relatively large ($a \gtrsim 0.1$ μm) silicate grains (Seab & Snow 1989).

If these results are typical, the O-rich stardust entering the ISM will tend to populate the upper range of the size distribution.

8.3 Stardust in Meteorites

8.3.1 Background

Our solar system was born some 4.568 Gyr ago. Its age is known rather precisely by means of radiometric dating techniques applied to samples of primitive meteorites (e.g., Bouvier & Wadhwa 2010). These fragments of asteroidal parent bodies formed at early times in the Sun's protoplanetary disk, and their radiometric ages refer to the epoch at which constituent minerals condensed. Most solids from the interstellar birth cloud had been vaporized and homogenized prior to recondensation, thereby erasing all chemical and mineralogical fingerprints of their presolar state. Exotic particles identified in the meteorites are exceptions: a tiny but highly significant population of survivors from the presolar interstellar medium, some of which predate the solar system's origin by at least a billion years (Heck et al. 2020).

Discovery of this population simultaneously answered a perceptive question posed many years previously ("Interstellar Grains in Museums?"; Cameron 1973) and instigated a new field ("Astrophysics with Extraterrestrial Materials"; review by Nittler & Ciesla 2016). A new window on cosmic chemical evolution was opened by the ability to apply advanced analytical techniques to physical samples of extrasolar dust in the laboratory (see Zinner et al. 2011 for a review of the relevant technology). Results have major implications for our understanding of the nature and origin of the dust itself and the nucleosynthetic processes that created its constituent elements. The field has been well-served by excellent review papers: see Anders & Zinner (1993), Zinner (1998), Hoppe (2011), and Davis (2011) in addition to those cited above.

Examples of stardust grains from meteorites are shown in Figure 8.14. Identification depends primarily on detailed isotopic analyses of samples extracted from carbonaceous chondrites, the least altered remnants of the protoplanetary disk. Solids that condensed locally have elemental and isotopic abundances that closely match those in the Sun (Section 7.1.3), whereas extrasolar grains (Table 8.2) display isotopic patterns that deviate from solar values to an extent that is incompatible with an origin in the solar system. The analytical techniques not only identify the particles as extrasolar but also provide evidence on their birth environment. Nuclear reactions in stars (Section 7.1) generate distinct isotopic abundance patterns according to physical conditions and the timescales on which they operate. Insight is often gained from trace impurity elements, including trapped noble gases, as well as from those that compose the bulk of a specific solid. Different patterns are predicted for certain elements depending on whether the reactions responsible proceed slowly during an extended phase of stellar evolution, or rapidly during a cataclysmic event. It is thus possible to distinguish stardust formed in (e.g.) the outflow of an AGB star from that formed in a supernova explosion. An example of such a diagnostic pattern is illustrated in Figure 8.15, and some properties of the various forms of stardust are summarized in Table 8.2.

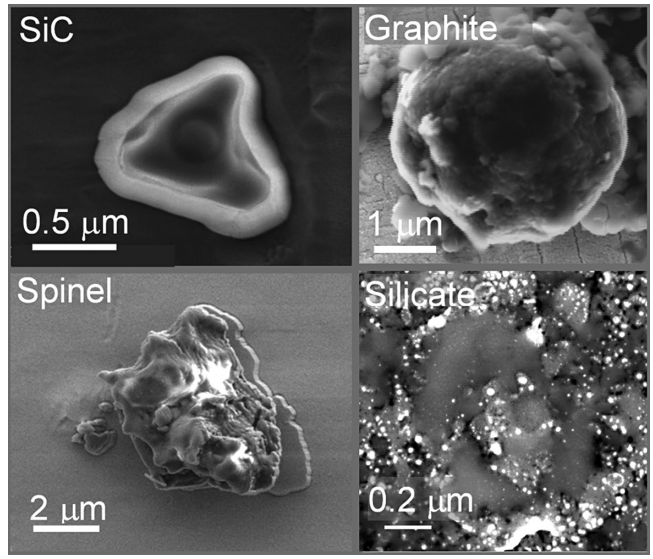

Figure 8.14. Examples of presolar grains identified in meteorites (Hoppe 2011). The grain labeled "silicate" (lower right) consists of an Al-rich core surrounded by a silicate mantle. The SiC grain originated in a supernova, the spinel ($MgAl_2O_4$) and silicate grains in AGB stars; the graphite grain could be of either AGB or supernova origin. Image credit: Max Planck Institute for Chemistry, courtesy of Peter Hoppe.

Table 8.2. Properties of Stardust Grains in Carbonaceous Chondrites.

Constituent	Grain Size (μm)	Abundance (ppm)	Stellar Sources
Silicates	$\lesssim$1	200	AGB, SNe (9:1)
Oxides	0.1–2	50	AGB, SNe (9:1)
SiC	0.3–50	30	AGB, SNe (20:1)
Si_3N_4	$\lesssim$1	0.002	SNe
Graphite	1–20	10	SNe, AGB (3:2)
Diamond	0.002	1400	SNe?
TiC	0.01–0.05	0.001	Similar to graphite

Notes: Abundances are in parts per million by mass relative to the bulk meteorite. Where two stellar sources are listed, a rough estimate of their relative numerical contributions is given. The presolar status of diamond is uncertain (see text). TiC is detected as subparticles within graphite rather than an independent population. Data are from Davis (2011) and references therein.

8.3.2 Composition and Origin: Carbon-rich Grains

The solar system is intrinsically oxygen-rich (C/O $\approx$ 0.5). Thus, we expect native mineral grains to consist mostly of oxygenated forms such as oxides and silicates, whereas carbonaceous forms such as graphite and silicon carbide are more likely to have originated elsewhere. This is largely confirmed by the investigations. Meteoritic

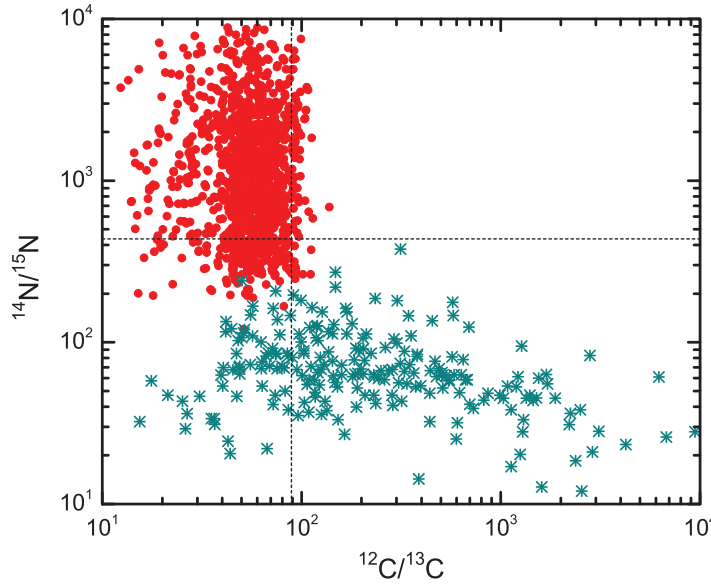

Figure 8.15. Stable isotope ratios for carbon versus nitrogen, comparing distributions for two classes of presolar silicon carbide grains: "mainstream" (red circles), and type X (asterisks), originating principally in AGB stars and core-collapse SNe, respectively. Dashed lines indicate mean solar values. Data are from the Presolar Grain Database (Stephan et al. 2020).

SiC, in particular, appears to be almost entirely extrasolar. Although by no means the most common, SiC is the most extensively studied of all forms of presolar dust, in part because its crystal structure accepts a number of trace elements in grains large enough to contain measurable quantities. They reveal orders-of-magnitude variations in isotopic abundances that allow the grains to be characterized into several groups (e.g., Davis 2011). Figure 8.15 compares stable isotope ratios for C and N in two such classes. The mainstream group, which accounts for about 90% of all SiC grains, exhibits a general pattern consistent with theoretical models and observed values for normal C-rich AGB stars of otherwise solar metallicity. In such stars, the CNO cycle in hydrogen-burning shells (Figure 8.3) controls the distribution of C versus N isotopes (e.g., Anders & Zinner 1993), such that grains from their outflows tend to cluster toward the upper left quadrant of Figure 8.15. The distribution of the rarer type X grains (1% to 2% of the sample) is dramatically different, with little or no overlap. Isotopic abundance patterns for these and other elements in type X SiC grains are consistent with an origin in the ejecta of core-collapse SNe. Similarly, the much rarer Si_3N_4 grains (Table 8.2) also exhibit a pattern indicative of an origin in SNe.

As well as establishing supernovae as the source, isotopic abundance patterns in X-type SiC grains also indicate a probable timescale for condensation (Liu et al. 2018). Grain formation in core-collapse SNe proceeds under conditions that evolve rapidly (Section 8.1.6). However, to make SiC in the outflow it is necessary to mix elements from different layers in the progenitor: Si and C are created by distinct processes, such

that the Si-rich zone is internal to the C-rich zone at the time of detonation. How long did this take? An answer is suggested by the abundances of certain trace elements in the grains that are products of extinct, short-lived radioactive nuclides produced in the explosion—effectively radiometric chronometers. By measuring the abundances of isotopes such as ^{49}Ti (the decay product of ^{49}V with a half-life 330 days), it is possible to constrain the time of formation. Liu et al. (2018) deduce that X-type SiC grains formed at least 2 years after their parent stars exploded, a result that places their origins in the mid-to-late phase of dust nucleation in core-collapse SNe (Sarangi & Cherchneff 2013). About two-thirds of all presolar graphite grains also display signatures of a supernova source, with abundance patterns similar to those of the SiC particles, suggesting a contemporary origin in the ejecta.

Presolar graphite grains display distinctive internal structures (Bernatowicz et al. 1991, 1996, 2005). Onion-like concentric layers of graphite may encase a core composed of PAH clusters or amorphous carbon, suggesting a formation sequence in which cores condense in isolation and then acquire graphitic mantles by vapor deposition in a C-rich atmosphere. The grains frequently contain much smaller particles (subgrains) embedded in the structure. Subgrains composed of TiC are common to graphites originating in both AGB stars and SNe (the compositions of other subgrains are different, with additional refractory carbides predominant in the former, pure metals in the latter; Croat et al. 2003, 2005). TiC particles embedded in the mantles must have formed prior to mantle deposition: their presence (and the absence of embedded carbides with lower condensation temperatures, such as SiC) places constraints on the condensation sequence. The density required, both to grow $>1\,\mu$m-sized grains within reasonable timescales and to explain the efficient inclusion of carbide crystals in the structure, is a factor $\sim$100 higher than would typically occur in a spherically symmetric wind, implying the occurrence of local high-density clumps in the outflows.

Another carbon-bearing candidate that might originate in SNe is diamond. Nanometer-sized diamond crystals (nanodiamonds) are abundant in carbonaceous chondrites (Table 8.2) and were among the first meteoritic grains to be proposed as presolar (Lewis et al. 1987). However, their status has since been questioned (e.g., Dai et al. 2002). Because they are so tiny (a nanodiamond of average size contains about 1800 carbon atoms), detailed isotopic analyses of trace elements that might confirm their origins cannot be performed on individual particles, and studies of aggregates yield ambiguous results. Mean isotopic ratios for elements such as C and N are close to solar (Davis 2011), but those of certain trace elements such as Xe suggest an extrasolar origin for some unknown fraction of the particles (see Lewis et al. 2020 for detailed discussion). It is difficult to understand how nanodiamonds could form in large numbers in a gas of solar composition, and their status thus remains unclear.

8.3.3 Composition and Origin: Oxygen-rich Grains

Identifying oxygen-rich presolar grains in meteorites is more challenging because they are composed of compounds similar to those formed in the solar nebula.

Indeed, the techniques commonly used to isolate refractory carbon grains often involve dissolving the dominant silicate component in acid, a process akin to "burning down a haystack to find the needle" (e.g., Nittler & Ciesa 2016). The development of advanced ion microprobe facilities capable of isotopic mapping with high spatial resolution enabled a different approach. This yielded the first detections of presolar silicates, identified in interplanetary dust particles by their anomalous isotopic oxygen compositions (Messenger et al. 2003). Application of this technique to meteorite sections led to the recognition of silicates and oxides as the most abundant presolar constituents (Table 8.2) if nanodiamonds are disregarded. As with C-rich particles, detailed studies of isotopic patterns allow insight into their origins: for example, the abundance ratios $^{17}O/^{16}O$ and $^{18}O/^{16}O$ are highly diagnostic (e.g., Hoppe 2011; Nittler & Ciesa 2016). The results identify some 10% of the sample as originating in SNe. A small fraction (< 1%) may originate in novae, but the majority formed in the outflows of AGB stars.

Presolar silicate grains contain a wide range of compounds and structures, with no obvious preference for any specific phase. Examples include single crystals of Mg_2SiO_4 or $MgSiO_3$, non-stoichiometric amorphous grains, and compound grains containing multiple minerals, including silicate/oxide aggregates (Nittler & Ciesla 2016; Nguyen et al. 2016). Mg silicates are dominant but some Fe-bearing compounds are also present, suggestive of non-equilibrium condensation. The crystalline fraction is about 40%. Presolar oxide grains include Al_2O_3 (corundum) and $MgAl_2O_4$ (spinel), often in the form of single crystals with structures and compositions consistent with equilibrium condensation. Thus, AGB stars appear capable of producing a range of oxidized phases under both equilibrium and non-equilibrium conditions. Identification of Al_2O_3 corroborates observational evidence for a probable contribution by this mineral to the mid-infrared spectra of AGB stars (Section 8.2.2). Crystallinity may be related to interstellar residence times prior to inclusion in the meteorites, given that interstellar silicates appear to be largely amorphized (Section 5.2.1).

8.3.4 Particle Sizes

It is interesting to compare sizes represented in the presolar grain population (Figure 8.14; Table 8.2) with those of interstellar particles, inferred from their optical properties. Presolar silicates have radii typically in the range $0.1 \lesssim a \lesssim 0.2$ μm, with a maximum of about 1 μm, broadly consistent with the silicate components of models for interstellar extinction and polarization (Sections 3.6.1 and 4.2.8). In notable contrast, presolar graphite grains identified in meteorites are enormously large compared with the graphitic nanoparticles proposed as carriers of the 217 nm absorption bump (Section 3.4), and larger, even, than particles invoked to account for the general extinction at longer wavelengths. This might seem perplexing, but there are reasons to suppose that the apparent size distribution of graphite in meteorites is skewed toward large grains and therefore unrepresentative

of the parent population. Smaller grains may have been destroyed selectively, prior to accretion into the meteorites, and further selection effects that tend to favor large grains may arise in the laboratory during the extraction process. Meteoritic graphite is, in fact, rare in terms of fractional mass—rarer, even, than SiC (Table 8.2), which is below detectable levels in the ISM (Section 5.2.2). The bulk of the C in carbonaceous chondrites is in organic refractory matter, which might have formed in part by surface reactions on graphite grains in the solar nebula (Barlow & Silk 1977), a process that would naturally tend to consume the smallest graphitic particles most efficiently (while leaving the more chemically-stable nanodiamonds intact). The discovery of large (>1 μm) particles of both graphite and SiC in meteorites is significant, nevertheless, for two reasons: (i) it demonstrates the occurrence of conditions in stellar outflows that enable growth to such sizes, as previously discussed; and (ii) it demonstrates that large grains do indeed exist in the ISM, even if they represent a mere "tip of the iceberg" with regard to the overall size distribution (see Sections 3.2.5, 3.6.1, and 8.4.2 for related discussions).

8.4 Stars as Sources of Interstellar Grains

Stardust undoubtedly contributes to the interstellar grain population. This is implied by observational evidence that evolved dust-forming stars may undergo rapid mass loss (see below), and confirmed by detections of presolar stardust in the solar system, discussed in the previous section. The mix of dust generated by a diverse population of stars includes both carbon-rich and oxygen-rich particles, in qualitative agreement with the need for both kinds of dust to exist in the ISM to account for its observed properties. The quantity of dust present in the ISM at any given time represents the balance between sources and sinks. This section attempts to assesses the significance of stardust as a source of interstellar dust.

8.4.1 Mass Loss

All mature stars lose mass to some degree, in the form of gaseous stellar winds driven by thermodynamic pressure. The flux of solar wind particles currently emanating from the Sun amounts to about 3×10^{-14} $M_\odot$ yr^{-1}, equivalent to a mere 0.03% of the total mass over its entire main-sequence lifetime. The flux correlates with stellar luminosity (L_*) and radius (R_*), so the mass loss rates of Sun-like stars increase dramatically during the red giant phase. The rate $\dot{M} = dM/dt$ for a star of mass $M = M_*$ arising from a thermally driven gaseous wind may be related to stellar parameters by the approximation

$$\dot{M} \approx 4 \times 10^{-13} \frac{L_*}{gR_*} \tag{8.4}$$

where $g = GM_*/R_*^2$ is the gravitational acceleration at the stellar surface and all quantities are expressed in solar units (Reimers 1975; Dupree 1986). Equation (8.4) thus predicts mass loss rates of $\dot{M} \sim 10^{-8}$ $M_\odot$ yr^{-1} for a first-ascent red (M-type) giant and $\dot{M} \sim 5 \times 10^{-7}$ $M_\odot$ yr^{-1} for a red supergiant; however, these values are

effectively lower limits for dust-producing stars because they do not take grain dynamics into account.

Cool stars with high mass loss rates invariably show evidence of dust in their envelopes, revealed most clearly by circumstellar infrared emission (Section 8.2.1). Grains nucleating in stellar atmospheres undergo outward acceleration due to radiation pressure, and transfer momentum to the gas by collisions. Empirical estimates of mass loss rates are based on observed expansion velocities in the gaseous outflows, in combination with measures of circumstellar mass, yielding results broadly consistent with detailed dynamical models that include the effect of radiation pressure on the dust (e.g., Bladh et al. 2019). Results for luminous stars with dusty envelopes show that mass loss rates increase with luminosity far more steeply than implied by Reimers' formula (see Höfner & Olofsson 2018 for a review). Values in the range 10^{-6}–10^{-4} $M_\odot\,yr^{-1}$ are typical of red supergiants (Jura & Kleinmann 1990) and both C-rich and O-rich AGB stars (Ramstedt et al. 2008; Eriksson et al. 2014; Bladh et al. 2019). A histogram for M-type stars over a range of evolutionary states (Figure 8.16) suggests a bimodal distribution, with peaks separated by two orders of magnitude. The highest rates may be attributed to dust-driven superwinds during the late phases of AGB evolution that precede ejection of a planetary nebula (Section 8.1.5). Such a star might lose a substantial fraction of its mass in a few thousand years.

That dust provides the impetus for such enhancements may be demonstrated by considering the balance between the forces of radiation pressure and gravity. Consider a spherical grain of mass m_d and radius a situated in a circumstellar shell

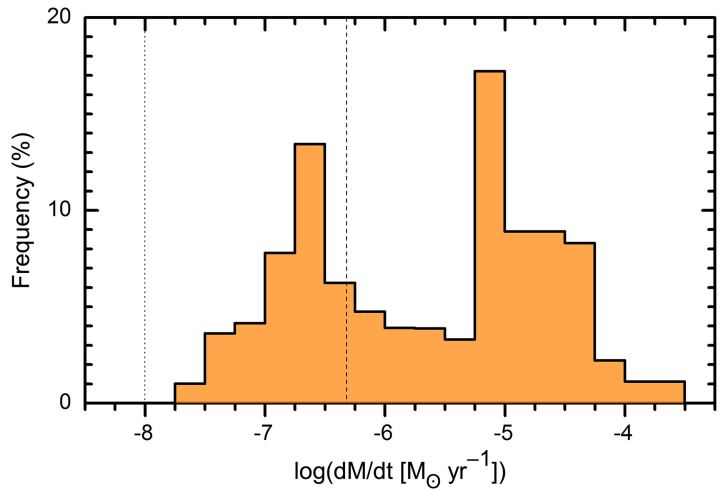

Figure 8.16. Histogram of observed mass loss rates in M-type luminous stars. The sample combines data for semi-regular variables, Miras, and OH/IR stars from Bladh et al. (2019) and references therein. Frequency as a percentage of the total corresponds to bins of width 0.25 dex in $\log(dM/dt)$. Vertical dotted and dashed lines correspond to values predicted by Reimers' formula (Equation (8.4)) for M-type giants and supergiants, respectively.

at a radial distance r from the center of a star. Let us assume that the circumstellar zone internal to the location of the grain is optically thin to stellar radiation, as expected near the inner boundary of the dust condensation region (Section 8.1.1). The outward force imposed by radiation pressure is then

$$F_{\rm pr} = \pi a^2 \langle Q_{\rm pr} \rangle \left(\frac{L_*}{4\pi r^2 c} \right) \tag{8.5}$$

where $Q_{\rm pr}$ is the efficiency factor for radiation pressure, defined in Section 2.4.1, and $\langle Q_{\rm pr} \rangle$ is its average value with respect to wavelength over the stellar spectrum. The opposing gravitational force is

$$F_{\rm gr} = \frac{G M_* m_{\rm d}}{r^2} \tag{8.6}$$

and we require $F_{\rm pr}/F_{\rm gr} > 1$ for outward acceleration. Combining Equations (8.5) and (8.6) and expressing $m_{\rm d}$ in terms of the density $\rho_{\rm s}$ of the solid grain material, this ratio is given by

$$\frac{F_{\rm pr}}{F_{\rm gr}} = \frac{3 L_*}{16 \pi G M_* c} \left\{ \frac{\langle Q_{\rm pr} \rangle}{a \rho_{\rm s}} \right\} \tag{8.7}$$

which is independent of r and varies with grain properties in proportion to the bracketed term on the right. $Q_{\rm pr}$ may be calculated as a function of wavelength for a given grain model using Mie theory (Section 2.1). It is typically maximized when $2\pi a/\lambda \sim 1$, and greater for strongly absorbing grains than for dielectric grains of the same size (because $Q_{\rm abs}$ is the dominant contributor to $Q_{\rm pr}$ for plausible values of the scattering asymmetry parameter; Section 2.4.1). As an example, Martin (1978) estimates $\langle Q_{\rm pr} \rangle \approx 0.18$ for graphite and 0.003 for silicates, assuming spheres of constant radius $a = 0.05$ μm in the atmosphere of a red giant of luminosity 10^4 $L_\odot$ and mass 4 $M_\odot$. It may be shown that dust is driven outward from red giants of luminosity $L_* \gtrsim 10^3$ $L_\odot$ for a range of grain size and composition. In the above example, $F_{\rm pr}$ exceeds $F_{\rm gr}$ by a factor of ~2000 for graphite grains and by a factor of ~40 for silicate grains (Equation (8.7)).

The spectrum of the radiation field naturally varies with r when the dust shell becomes optically thick, shifting the peak from the near-infrared (typical of an M-type photosphere) to the mid-infrared at large distances from the star, as radiation is absorbed and reradiated by warm circumstellar dust. This change is unlikely to inhibit the outward flow of the particles, given that both carbon and silicate grains are efficient absorbers in the mid-infrared. The outward speeds of the grains are limited primarily by frictional drag exerted by collisions with the gas. Grain speeds cannot be measured directly but may become coupled with those of the gas in dense regions of the outflow. Typical gaseous wind speeds, determined by the Doppler method, are in the range 5–30 km s^{-1}, values that exceed the local escape velocity at sufficiently large distances from the star.

8.4.2 Predicting the Size Distribution

The terminal speed of a particle driven through a gas by radiation pressure depends on its size, such that large grains tend to overtake smaller ones, resulting in grain–grain collisions. Depending on their relative speeds, the impacts might be constructive (resulting in coagulation) or destructive (resulting in fragmentation). The influence of collisions on the size distribution of the particles in red giant winds and planetary nebulae is assessed by Biermann & Harwit (1980). Frequent collisions at relative speeds $\gtrsim$1 km s^{-1} are predicted, resulting in the imposition of a power-law form for the size distribution, independent of the initial size distribution of the condensates. On the basis of fragmentation theory (originally applied to asteroids), Biermann and Harwit argue that the emergent grains follow a size distribution of the form $n(a) \propto a^{-3.5}$. This model suggests a physical basis for the origin of the interstellar grain-size distribution, deduced by fitting the extinction curve (Section 3.6.1).

A parameter relevant to calculations of interstellar extinction that must be reconciled with empirical evidence from stardust is the upper bound of the grain radius, $a_{\rm max}$. In early work, fixed upper bounds of $a_{\rm max} \sim 0.2$ (silicates) and ~ 1 μm (graphite) were typical of models generating acceptable fits to the diffuse-ISM extinction curve using the power-law form for the distribution function (Equation (3.30)). However, a smooth decline in $n(a)$ with increasing a is more physically plausible, and we have proof from studies of meteorites that some of the dust grains injected into the ISM from evolved stars are much larger than these limits (Section 8.3.4). A functional form that accommodates this is

$$n(a) \propto a^{-3.5} \exp(-a/a_0) \tag{8.8}$$

where the parameter a_0 specifies a characteristic size, such that power-law behavior is retained for $a \ll a_0$, and there is no specific cut-off for $a \gg a_0$. The observed properties of both C-rich and O-rich mass-losing red giants are consistent with a size distribution of this form with $0.10 \lesssim a_0 \lesssim 0.15$ μm (Jura 1994, 1996), similar to values obtained from fits to interstellar extinction (Kim et al. 1994).

8.4.3 Dust-to-Gas Ratios

In principle, the mass ratio of dust to gas ($Z_{\rm d}$) in a circumstellar outflow may be determined simply by comparing independent measures of the mass loss rates for dust and for gas. The mass of dust may be estimated from observations of far-infrared continuum emission, that of gas from millimeter-wave CO line emission (see Knapp 1985 and Olofsson et al. 1993 for technical details). Results are subject to substantial uncertainty because relevant parameters are either unknown or not tightly constrained. The terminal speed of the dust cannot be measured directly and is therefore assumed to be tied to that of the gas, and the reliability of this assumption is likely to depend on the evolutionary status of the star and its mass loss rate. Also, because the principal gaseous component is not generally accessible to direct measurement, the mass of gas is subject to uncertainties in the CO/H ratio. See the review by Höfner & Olofsson (2018) for further discussion and caveats.

Another important variable is the initial metallicity of the star. A general increase in Z_d with metallicity is expected, and this is confirmed by comparisons of data for AGB stars in the Milky Way and the Magellanic Clouds (van Loon 2000). Metallicity is fundamental to oxygen-rich dust production because elemental Mg, Si, and Fe are not synthesized on the AGB. Thus, an M-type star must rely on its initial endowment of these elements—i.e., on its metallicity—to make silicates and oxides, whereas a carbon star generates its own primary condensate. However, the dominant factor determining Z_d in carbon stars is the C/O ratio (Eriksson et al. 2014), and this depends on both initial metallicity and evolutionary status.

Observational estimates of dust-to-gas ratios in AGB outflows generally fall within the range $10^{-3} \lesssim Z_d \lesssim 10^{-2}$ (e.g., Knapp 1985; Olofsson et al. 1993; Justtanont et al. 1994; Ramstedt et al. 2008). Results for planetary nebulae are typically of the same order (Stasinska & Szczerba 1999). The upper end of this range extends to values that are comparable with results for the diffuse ISM (Sections 3.2.6 and 7.2.2) but higher than predictions based on models for dust production in either C-type and M-type stars ($Z_d \lesssim 3 \times 10^{-3}$; Eriksson et al. 2014; Bladh et al. 2019). Z_d falls well below theoretical upper limits for a given metallicity because significant proportions of elemental C and O remain in the gas.

8.4.4 Production and Destruction Timescales

The contribution of stardust to the overall dust content of a galaxy may be assessed by comparing the rate of production, summed over all relevant sources, with the rate of destruction in the interstellar medium. This is a complex task that depends on many parameters, some of which are not well constrained. The primary stellar sources are considered to be AGB stars and core-collapse supernovae, which correspond to the most productive phases of dust formation for intermediate and high mass stars, as previously discussed. Other types of star and other evolutionary phases are known to make dust, but their net contributions are considered to be negligible because their populations and/or production rates are relatively small. For example, the contribution from red supergiants is estimated to be no more than a few percent of that from AGB stars (Massey et al. 2005). Therefore, only AGB stars and core-collapse SNe are considered here.

The overall rate at which stardust is injected into the ISM of a galaxy may be stated as

$$[\dot{M}_G]_d = \sum_{AGB} \dot{M}_d \; + \; \sum_{SNe} \dot{M}_d \tag{8.9}$$

where $\dot{M}_d = \dot{M}\ Z_d$ is the mean mass loss rate for dust flowing from each individual star. The summation for supernovae may be approximated by $f\,\Delta m_d$, where f is the mean frequency of core-collapse events in the galaxy ($\sim$ 2 per century for those similar to the Milky Way), and Δm_d is the average dust mass injected into the ISM per event. The ideal way to evaluate the total for AGB stars would be to detect the entire population, estimate the dust-injection rate of each star individually, and sum the results. A complete census of dust-forming stars in the Milky Way is not possible

because of source confusion and high extinction in the galactic disk, but can be attempted for nearby dwarf galaxies such as the Magellanic Clouds (e.g., Schneider et al. 2014). A more feasible approach is to combine estimates of the space densities of dust-forming stars with average values of $\dot{M}_{\rm d}$ to evaluate the injection rate in a specific galactic region such as the solar neighborhood (Gehrz 1989).

Intricate models have been developed that link dust production to the stellar initial mass function (IMF), star formation history and evolving metallicity of a galaxy, with a view to understanding the significance of stardust not only in the Milky Way and its near neighbors but also in galaxies at high redshift. Examples from an extensive literature include Dwek (1998), Ferrarotti & Gail (2006), Zhukovska et al. (2008), Zhukovska & Henning (2013), Ventura et al. (2014), McKinnon et al. (2016, 2017), Ginolfi et al. (2018), and Nanni et al. (2020). The IMF specifies the relative numbers of stars born within a given mass range: for stars relevant to this discussion ($M_* \gtrsim 0.8$ M$_\odot$), the IMF varies as $M_*^{-\alpha}$ where $\alpha \approx 2.35$ (Salpeter 1955). The timescale for a star to reach its epoch of optimal dust production is of the same order as its main-sequence lifetime ($\sim 10^{10} M_*^{-2.5}$ years with M_* in solar units), and this ranges from a few million years for massive supernova progenitors to times approaching the age of the universe for the least massive stars considered. Thus, a period of intense star formation activity instigates a rapid onset of dust production by supernovae and the most massive AGB stars, consistent with observational evidence for dust in high-redshift galaxies. This is followed by sustained production on longer timescales as less massive stars reach the AGB. Dust yields are closely linked to metallicity, both spatially within a galaxy such as the Milky Way and from one galaxy to another. As carbon stars have relatively low mass ($\sim$ 2 M$_\odot$), C-rich grain production lags behind O-rich grain production if AGB stars are the primary source.

An important metric constrained by the models is the timescale for dust production in stars relative to the existing dust content of a galaxy. A calculation for the solar region of the Milky Way is informative. Consider a column of cross-sectional area $A_{\rm G}$ with its axis perpendicular to the galactic disk at the solar location. The stardust production rate per unit cross-section is then $[\dot{M}_{\rm G}]_{\rm d}/A_{\rm G}$, summed for the two source types (Equation (8.9)). Taking their space density, mass loss rates, and dust-to-gas ratios into account, an estimate of the total from AGB stars is

$$\left[\frac{[\dot{M}_{\rm G}]_{\rm d}}{A_{\rm G}}\right]_{\rm AGB} \sim \; 8 \times 10^{-6} \;\; {\rm M}_\odot \, {\rm kpc}^{-2} {\rm yr}^{-1} \tag{8.10}$$

(Jones 1997; Tielens 2012), to which O-rich and C-rich sources contribute approximately in the ratio 3:1. The global average rate for dust production in supernovae is

$$\left[\frac{[\dot{M}_{\rm G}]_{\rm d}}{A_{\rm G}}\right]_{\rm SNe} = \frac{f \, \Delta m_{\rm d}}{\pi R_{\rm G}^2} \lesssim 14 \times 10^{-6} \;\; {\rm M}_\odot \, {\rm kpc}^{-2} {\rm yr}^{-1} \tag{8.11}$$

where $R_{\rm G} \approx 15$ kpc is the radius of the (stellar) galactic disk, and the expected frequency is $f \approx 0.02$ yr^{-1}. By far the greatest source of uncertainty in the estimate

for SNe is the mass of dust produced per event: the above calculation assumes $\Delta m_{\rm d} \lesssim 0.5$ M$_\odot$, consistent with relatively high estimates for SN 1987A and Cassiopeia A (Section 8.2.1) but allowing for the possibility that typical values may be significantly lower (Tielens 2012; Bocchio et al. 2016; Ginolfi et al. 2018). Context for these numbers is provided by an estimate of the mass of dust currently present in the ISM, enabling the timescale required to produce an equivalent mass to be calculated. Combining the observed column mass density of neutral (diffuse) gas in the solar neighborhood (~ 8 M$_\odot$ pc^{-2}; Gilmore & Zeilik 2000) with a mean dust-to-gas ratio of $Z_{\rm d} \sim 5 \times 10^{-3}$ for the diffuse ISM (Table 7.2, assuming intermediate depletion), the column mass density of dust is $[M_{\rm G}]_{\rm d}/A_{\rm G} \sim 4 \times 10^4$ M$_\odot$ kpc^{-2}. The resultant timescale is then the ratio of this estimate and the summed production rates (Equations (8.10) and (8.11)):

$$\tau_{\rm sd} = \frac{[M_{\rm G}]_{\rm d}}{[\dot{M}_{\rm G}]_{\rm d}} \gtrsim 2 \ \ {\rm Gyr}. \tag{8.12}$$

On reaching the ISM, stardust grains are "subject to a variety of indignities" (Seab 1988), of which sputtering in supernova-generated shock waves (Section 9.1.2) is the most severe. This occurs mainly in low-density phases of the ISM on timescales that may be estimated with reference to physical models describing the process. A global mean destruction rate is determined for an effective supernova frequency, adjusted to allow for the fact that SNe tend to occur in associations rather than in isolation (the same grain cannot be destroyed multiple times!). The corresponding timescale is then estimated in a manner analogous to the stardust calculation above (total mass divided by destruction rate), in effect the timescale ($\tau_{\rm sh}$) for shocks to destroy all the dust in a galaxy if no new dust were being produced.

The results have created a dilemma. It was concluded in early work that $\tau_{\rm sh} \lesssim 0.5$ Gyr for both silicate and carbon dust in our Galaxy (see Jones & Nuth 2011 for a review). If so, interstellar dust is destroyed by shocks far more rapidly than it is replenished by stellar mass loss ($\tau_{\rm sh} \ll \tau_{\rm sd}$). It is then challenging to account for the origin of the dust currently observed in the ISM, and it is also difficult to understand how large stardust grains, some of which predate the birth of the solar system by a billion years (Section 8.3), could have survived long enough to find their way into our meteorite collection (Slavin et al. 2004). More recent models, based on potentially more realistic assumptions, may have mitigated this discrepancy somewhat, suggesting that $\tau_{\rm sh} \sim \tau_{\rm sd}$ is within the range of uncertainty (Slavin et al. 2015; Priestley et al. 2020).

The proportion of all interstellar dust originating in stellar outflows remains an open question, but there is general agreement that a substantial fraction must be formed by interstellar rather than circumstellar processes. For example, limits on the abundance of SiC (Section 5.2.2) suggest that carbon stars may not be the dominant source of C-rich dust (Chen et al. 2022). Because densities are low, even in "dense" clouds, formation of solids in the ISM must proceed by gradual deposition of matter onto the surfaces of existing grains rather than by nucleation of new particles. We know from depletion data (Chapter 7) that gas and dust exchange material in the

diffuse ISM at a density-dependent rate, and we know from studies of spectral features (Chapter 5) that grains acquire icy mantles in dense clouds. Feasible routes to carbonaceous dust production might thus include direct deposition of C atoms onto refractory dust, or photolytic processing of ice mantles.

An interstellar route to *silicate* dust production is harder to envisage. Abundance limits on Si and Mg require that these elements remain mostly sequestered in amorphous silicates to explain the strengths and profiles shapes of the infrared spectral features (Sections 5.2.1 and 7.3.2). Si, Mg, and Fe atoms released to the gas by destruction of stardust in shocks may subsequently reoxidize and reattach to grain surfaces, but it is unclear how they could assemble into silicate compounds consistent with the observed properties of the dust under interstellar conditions. Recombination in an annealed ice matrix has been proposed, supported by laboratory simulations (Rouillé et al. 2020), but the efficiency of this process is not yet known. A related issue is the need for the silicates to remain largely distinct from the carbon population to explain differences in their response to alignment (Section 4.2.7); this seems improbable if most of the dust is reprocessed in the ISM, as the Si-rich and C-rich components would tend to become blended.

To summarize, it seems hard to avoid the conclusion that circumstellar environments around O-rich stars are by far the most efficient and effective sites for silicate dust production (Section 8.1.3). It may be relevant to recall that such environments arise during the earliest as well as the latest stages of stellar evolution (the phase diagram in Figure 8.4 is applicable to both situations for solar metallicity). It was suggested many years ago that star formation might be a significant *source* of interstellar dust (Herbig 1970; Burke & Silk 1976). Silicates readily condense and grow in a protoplanetary disk, thereby forming minerals that we now find in interplanetary dust, in stony meteorites, and in the ground beneath our feet. As a young star approaches the main sequence, it generates a wind that disperses solid particles that failed to accrete into larger bodies, driven mainly by radiation pressure. Of course, we should not necessarily expect the star formation process to be a net producer of dust: it may consume at least as much as it creates, given that the condensible elements are likely to be substantially depleted into solids prior to collapse of the birth cloud. But it can alter the *quality* of the dust that gets recycled to the ISM, for example by vaporizing coatings of randomly accreted Si, Mg, and Fe atoms, and recondensing them into real silicates. Although largely ignored in subsequent decades, this is an idea worth reconsidering.

References

Abia, C., de Laverny, P., Cristallo, S., Kordopatis, G., & Straniero, O. 2020, A&A, 633, A135
Agúndez, M., Martínez, J. I., de Andres, P. L., Cernicharo, J., & Martín-Gago, J. A. 2020, A&A, 637, A59
Anders, E., & Zinner, E. 1993, Metic, 28, 490
Arendt, R. G., Dwek, E., Bouchet, P., et al. 2016, AJ, 151, 62
Barlow, M. J., & Silk, J. 1977, ApJ, 215, 800
Barshay, S. S., & Lewis, J. S. 1976, ARA&A, 14, 81
Begemann, B., Dorschner, J., Henning, T., et al. 1997, ApJ, 476, 199

Bernatowicz, T. J., Amari, S., Zinner, E. K., & Lewis, R. S. 1991, ApJ, 373, L73
Bernatowicz, T. J., Cowsik, R., Gibbons, P. C., et al. 1996, ApJ, 472, 760
Bernatowicz, T. J., Akande, O. W., Croat, T. K., & Cowsik, R. 2005, ApJ, 631, 988
Biermann, P., & Harwit, M. 1980, ApJ, 241, L105
Bladh, S., Liljegren, S., Höfner, S., Aringer, B., & Marigo, P. 2019, A&A, 626, A100
Bocchio, M., Marassi, S., Schneider, R., et al. 2016, A&A, 587, A157
Bode, M. F. 1988, in Dust in the Universe, ed. M. E. Bailey, & D. A. Williams (Cambridge: Cambridge Univ. Press), 73
Bode, M. F. 2010, AN, 331, 160
Boogert, A. C. A., Gerakines, P. A., & Whittet, D. C. B. 2015, ARA&A, 53, 541
Bouchet, P., Dwek, E., Danziger, J., et al. 2006, ApJ, 650, 212
Bouvier, A., & Wadhwa, M. 2010, NatGe, 3, 637
Burke, J. R., & Silk, J. 1976, ApJ, 210, 341
Buss, R. H., & Snow, T. P. 1988, ApJ, 335, 331
Buss, R. H., Lamers, H. J. G. L. M., & Snow, T. P. 1989, ApJ, 347, 977
Cameron, A. G. W. 1973, in IAU Symp. 52, Interstellar Dust & Related Topics, ed. J. M. Greenberg, & H. C. van de Hulst (Dordrecht: Reidel), 545
Chen, T., Xiao, C. Y., Li, A., & Zhou, C. T. 2022, MNRAS, 509, 5231
Chiar, J. E., Tielens, A. G. G. M., Adamson, A. J., & Ricca, A. 2013, ApJ, 770, 78
Cigan, P., Matsuura, M., Gomez, H. L., et al. 2019, ApJ, 886, 51
Clayton, D. D. 2013, ApJ, 762, 5
Croat, T. K., Bernatowicz, T., Amari, S., Messenger, S., & Stadermann, F. J. 2003, GeCoA, 67, 4705
Croat, T. K., Stadermann, F. J., & Bernatowicz, T. J. 2005, ApJ, 631, 976
Cox, N. L. J., Kerschbaum, F., van Marle, A.-J., et al. 2012, A&A, 537, A35
Dai, Z. R., Bradley, J. P., Joswiak, D. J., et al. 2002, Natur, 418, 157
Davis, A. M. 2011, PNAS, 108, 19142
De Looze, I., Barlow, M. J., Swinyard, B. M., et al. 2017, MNRAS, 465, 3309
De Looze, I., Barlow, M. J., Bandiera, R., et al. 2019, MNRAS, 488, 164
DePew, K., Speck, A., & Dijkstra, C. 2006, ApJ, 640, 971
Donn, B., & Nuth, J. A. 1985, ApJ, 288, 187
Dorschner, J., Begemann, B., Henning, T., Jäger, C., & Mutschke, H. 1995, A&A, 300, 503
Douvion, T., Lagage, P. O., Cesarcky, C. J., & Dwek, E. 2001, A&A, 373, 281
Draine, B. T. 1984, ApJ, 277, L71
Draine, B. T. 2016, ApJ, 831, 109
Drilling, J. S., Hecht, J. H., Clayton, G. C., et al. 1997, ApJ, 476, 865
Dupree, A. K. 1986, ARA&A, 24, 377
Dwek, E. 1998, ApJ, 501, 643
Dwek, E. 2016, ApJ, 825, 136
Dwek, E., & Arendt, R. G. 2015, ApJ, 810, 75
Dwek, E., Sarangi, A., & Arendt, R. G. 2019, ApJ, 871, L33
Eriksson, K., Nowotny, W., Höfner, S., Aringer, B., & Wachter, A. 2014, A&A, 566, A95
Fabian, D., Jäger, C., Henning, T., Dorschner, J., & Mutschke, H. 2000, A&A, 364, 282
Ferrarotti, A. S., & Gail, H.-P. 2006, A&A, 447, 553
Frenklach, M., & Feigelson, E. D. 1989, ApJ, 341, 372
Gail, H.-P., & Sedlmayr, E. 1986, A&A, 166, 225

Gail, H.-P., & Sedlmayr, E. 1987, in Physical Processes in Interstellar Clouds, ed. G. E. Morfill, & M. Scholer (Dordrecht: Reidel), 275
Gail, H.-P., Wetzel, S., Pucci, A., & Tamanai, A. 2013, A&A, 555, A119
Gail, H.-P., Scholz, M., & Pucci, A. 2016, A&A, 591, A17
Gehrz, R. D. 1989, in IAU Symp. 135, Interstellar Dust, ed. L. J. Allamandola, & A. G. G. M. Tielens (Dordrecht: Kluwer), 445
Gehrz, R. D., Truran, J. W., Williams, R. E., & Starrfield, S. 1998, PASP, 110, 3
Gilmore, G. F., & Zeilik, M. 2000, in Allen's Astrophysical Quantities, ed. A. N. Cox (4th ed.; New York: Springer), 471
Ginolfi, M., Graziani, L., Schneider, R., et al. 2018, MNRAS, 473, 4538
Golriz, S. S., Blommaert, J. A. D. L., Vanhollebeke, E., et al. 2014, MNRAS, 443, 3402
Groenewegen, M. A. T. 1997, A&A, 317, 503
Groenewegen, M. A. T. 2012, A&A, 543, A36
Groenewegen, M. A. T., & Sloan, G. C. 2018, A&A, 609, A114
Groenewegen, M. A. T., Whitelock, P. A., Smith, C. H., & Kerschbaum, F. 1998, MNRAS, 293, 18
Guélin, M., Patel, N. A., Bremer, M., et al. 2018, A&A, 610, A4
Guerrero, M. A., & Ortiz, R. 2020, MNRAS, 491, 680
Hecht, J. H. 1986, ApJ, 305, 817
Hecht, J. H. 1991, ApJ, 367, 635
Hecht, J. H., Holm, A. V., Donn, B., & Wu, C. C. 1984, ApJ, 280, 228
Heck, P. R., Greer, J., Kööp, L., et al. 2020, PNAS, 117, 1884
Henning, Th. 2010, ARA&A, 48, 21
Henning, Th., Begemann, B., Mutschke, H., & Dorschner, J. 1995, A&AS, 112, 143
Herbig, G. H. 1970, Mémoires de la Société Royale des Sciences de Liège, 19, 13
Höfner, S., & Olofsson, H. 2018, A&ARv, 26, 1
Hoppe, P. 2011, in 11th Symp. on Nuclei in the Cosmos, ed. K. Blaum, N. Christlieb, & G. Martinez-Pinedo, https://pos.sissa.it/100/021/
Hrivnak, B. J., Volk, K., & Kwok, S. 2000, ApJ, 535, 275
Iben, I., & Renzini, A. 1983, ARA&A, 21, 271
Jäger, C., Molster, F. J., Dorschner, J., et al. 1998, A&A, 339, 904
Johnson, J. A. 2019, Sci, 363, 474
Jones, A. P. 1997, in ASP Conf. Ser. 122, From Stardust to Planetesimals, ed. Y. J. Pendleton, & A. G. G. M. Tielens (San Francisco, CA: ASP), 97
Jones, A. P., & Nuth, J. A. 2011, A&A, 530, 44
Jones, O. C., Kemper, F., Sargent, B. A., et al. 2012, MNRAS, 427, 3209
Jura, M. 1994, ApJ, 434, 713
Jura, M. 1996, ApJ, 472, 806
Jura, M. 1999, ApJ, 515, 706
Jura, M., & Kleinmann, S. G. 1990, ApJS, 73, 769
Justtanont, K., Skinner, C. J., & Tielens, A. G. G. M. 1994, ApJ, 435, 852
Justtanont, K., Skinner, C. J., Tielens, A. G. G. M., Meixner, M., & Baas, F. 1996, ApJ, 456, 337
Kastner, J. H., Zijlstra, A., Balick, B., & Sahai, R. 2018, in ASP Conf. Ser. 517, Science with a Next Generation Very Large Array, ed. E. Murphy (San Francisco, CA: ASP), 395
Kastner, J. H., Moraga, P., Balick, B., Bublitz, J., Montez, R., Frank, A., & Blackman, E. 2022, ApJ, 927, 100
Kim, S. H., Martin, P. G., & Hendry, P. D. 1994, ApJ, 422, 164

Kimura, Y., Tanaka, K. K., Nozawa, T., Takeuchi, S., & Inatomi, Y. 2017, SciA, 3, e1601992
Knapp, G. R. 1985, ApJ, 293, 273
Kotak, R., Meikle, W. P. S., Farrah, D., et al. 2009, ApJ, 704, 306
Kwitter, K. B., & Henry, R. B. C. 2022, PASP, 134, 022001
Kwon, Y.-J., & Suh, K.-W. 2014, JKAS, 47, 123
Lewis, J. B., Floss, C., Isheim, D., et al. 2020, M&PS, 55, 1382
Lewis, R. S., Tang, M., Wacker, J. F., Anders, E., & Steel, E. 1987, Natur, 326, 160
Little-Marenin, I. R. 1986, ApJ, 307, L15
Liu, J., Jiang, B. W., Li, A., & Gao, J. 2017, MNRAS, 466, 1963
Liu, N., Nittler, L. R., Alexander, C. M. O'D., & Wang, J. 2018, SciA, 4, 1054
Lodders, K. 2003, ApJ, 591, 1220
Lodders, K., & Fegley, B. 1995, Metic, 30, 661
Malek, S. E., & Cami, J. 2014, ApJ, 780, 41
Martin, P. G. 1978, Cosmic Dust, its Impact on Astronomy (Oxford: Oxford Univ. Press)
Martin, P. G., & Rogers, C. 1987, ApJ, 322, 374
Massey, P., Plez, B., Levesque, E. M., et al. 2005, ApJ, 634, 1286
Matsuura, M., Dwek, E., Meixner, M., et al. 2011, Sci, 333, 1258
McKinnon, R., Torrey, P., & Vogelsberger, M. 2016, MNRAS, 457, 3775
McKinnon, R., Torrey, P., Vogelsberger, M., Hayward, C., & Marinacci, F. 2017, MNRAS, 468, 1505
Messenger, S., Keller, L. P., Stadermann, F. J., Walker, R. M., & Zinner, E. 2003, Sci, 300, 105
Messenger, S. J., Speck, A., & Volk, K. 2013, ApJ, 764, 142
Micelotta, E. R., Matsuura, M., & Sarangi, A. 2018, SSRv, 214, 53
Mishra, A., Li, A., & Jiang, B. W. 2015, ApJ, 802, 39
Mishra, A., Li, A., & Jiang, B. W. 2016, ApJ, 825, 68
Montiel, E. J., Clayton, G. C., Sugerman, B. E. K., et al. 2018, AJ, 156, 148
Muci, A. M., Blanco, A., Fonti, S., & Orofino, V. 1994, ApJ, 436, 831
Mutschke, H., Begemann, B., Dorschner, J., et al. 1998, A&A, 333, 188
Mutschke, H., Andersen, A. C., Clément, D., Henning, Th., & Peiter, G. 1999, A&A, 345, 187
Nanni, A., Bressan, A., Marigo, P., & Girardi, L. 2013, MNRAS, 434, 2390
Nanni, A., Burgarella, D., Theulé, P., Côté, B., & Hirashita, H. 2020, A&A, 641, A168
Nguyen, A. N., Keller, L. P., & Messenger, S. 2016, ApJ, 818, 51
Nittler, L. R., & Ciesla, F. 2016, ARA&A, 54, 53
Nuth, J. A. 1996, in The Cosmic Dust Connection, ed. J. M. Greenberg (Dordrecht: Kluwer), 205
Olofsson, H., Eriksson, K., Gustafsson, B., & Carlström, U. 1993, ApJS, 87, 267
Onaka, T., de Jong, T., & Willems, F. J. 1989, A&A, 218, 169
Paquette, J. A., & Nuth, J. A. 2011, ApJ, 737, L6
Posch, T., Kerschbaum, F., Mutschke, H., Dorschner, J., & Jäger, C. 2002, A&A, 393, L7
Priestley, F. D., Chawner, H., Matsuura, M., et al. 2020, MNRAS, 500, 2543
Ramstedt, S., Schöier, F. L., Olofsson, H., & Lundgren, A. A. 2008, A&A, 487, 645
Reimers, D. 1975, Memoires of the Societe Royale des Sciences de Liege, 8, 369
Rietmeijer, F. J. M., Nuth, J. A., & Karner, J. M. 1999, ApJ, 527, 395
Rouillé, G., Jäger, C., & Henning, T. 2020, ApJ, 892, 96
Salpeter, E. E. 1955, ApJ, 121, 161
Salpeter, E. E. 1974, ApJ, 193, 579
Salpeter, E. E. 1977, ARA&A, 15, 267

Santoro, G., Martinez, L., Lauwaet, K., et al. 2020, ApJ, 895, 97
Sarangi, A., & Cherchneff, I. 2013, ApJ, 776, 107
Sarangi, A., Matsuura, M., & Micelotta, E. R. 2018, SSRv, 214, 63
Schneider, R., Valiante, R., Ventura, P., et al. 2014, MNRAS, 442, 1440
Seab, C. G. 1988, in Dust in the Universe, ed. M. E. Bailey, & D. A. Williams (Cambridge: Cambridge Univ. Press), 303
Seab, C. G., & Snow, T. P. 1989, ApJ, 347, 479
Shepard, L. M., & Speck, A. K. 2021, MNRAS, 506, 4750
Slavin, J. D., Jones, A. P., & Tielens, A. G. G. M. 2004, ApJ, 614, 796
Slavin, J. D., Dwek, E., & Jones, A. P. 2015, ApJ, 803, 7
Sloan, G. C., & Price, S. D. 1998, ApJS, 119, 141
Sloan, G. C., Kraemer, K. E., Goebel, J. H., & Price, S. D. 2003, ApJ, 594, 483
Smith, R. G., Sellgren, K., & Tokunaga, A. T. 1988, ApJ, 334, 209
Snow, T. P., Buss, R. H., Gilra, D. P., & Swings, J. P. 1987, ApJ, 321, 921
Speck, A. K., Whittington, A. G., & Tartar, J. B. 2008, ApJ, 687, L91
Speck, A. K., Corman, A. B., Wakeman, K., Wheeler, C. H., & Thompson, G. 2009, ApJ, 691, 1202
Stasinska, G., & Szczerba, R. 1999, A&A, 352, 297
Stephan, T., Bose, M., Boujibar, A., et al. 2020, LPSC, 51, 2140
Thompson, G. D., Corman, A. B., Speck, A. K., & Dijkstra, C. 2006, ApJ, 652, 1654
Tielens, A. G. G. M. 2008, ARA&A, 46, 289
Tielens, A. G. G. M. 2012, in IAU Symp. 284, The Spectral Energy Distribution of Galaxies, ed. R. J. Tuffs, & C. C. Popescu (Cambridge: Cambridge Univ. Press), 72
van Loon, J. Th. 2000, A&A, 354, 125
Ventura, P., Dell'Agli, F., Schneider, R., et al. 2014, MNRAS, 439, 977
Waters, L. B. F. M., Waelkens, C., van Winckel, H., et al. 1998, Natur, 391, 868
Whitney, B. A., Balm, S. P., & Clayton, G. C. 1993, in ASP Conf. Ser. 45, Luminous High-Latitude Stars, ed. D. D. Sasselov (San Francisco, CA: ASP), 115
Willems, F. J., & de Jong, T. 1986, A&A, 309, L39
Williams, B. J., Borkowski, K. J., Reynolds, S. P., et al. 2012, ApJ, 755, 3
Wooden, D. H., Rank, D. M., Bregman, J. D., et al. 1993, ApJS, 88, 477
Zhang, Y. 2020, ApJ, 898, 151
Zhukovska, S., & Henning, T. 2013, A&A, 555, A99
Zhukovska, S., Gail, H.-P., & Trieloff, M. 2008, A&A, 479, 453
Zijlstra, A. A., Loup, C., Waters, L. B. F. M., & de Jong, T. 1992, A&A, 265, L5
Zinner, E. 1998, AREPS, 26, 147
Zinner, E. K., Moynier, F., & Stroud, R. M. 2011, PNAS, 108, 19135